© 2022. Published by The Company of Biologists Ltd | Development (2022) 149, dev199726. doi:10.1242/dev.199726

RESEARCH ARTICLE

Transmural pressure signals through retinoic acid to regulate lung branching

Jacob M. Jaslove[1,2], Katharine Goodwin[3], Aswin Sundarakrishnan[4], James W. Spurlin, III[4,5], Sheng Mao[6,7], Andrej Košmrlj[7,8] and Celeste M. Nelson[1,4,*]

ABSTRACT

During development, the mammalian lung undergoes several rounds of branching, the rate of which is tuned by the relative pressure of the fluid within the lumen of the lung. We carried out bioinformatics analysis of RNA-sequencing of embryonic mouse lungs cultured under physiologic or sub-physiologic transmural pressure and identified transcription factor-binding motifs near genes whose expression changes in response to pressure. Surprisingly, we found retinoic acid (RA) receptor binding sites significantly overrepresented in the promoters and enhancers of pressure-responsive genes. Consistently, increasing transmural pressure activates RA signaling, and pharmacologically inhibiting RA signaling decreases airway epithelial branching and smooth muscle wrapping. We found that pressure activates RA signaling through the mechanosensor Yap. A computational model predicts that mechanical signaling through Yap and RA affects lung branching by altering the balance between epithelial proliferation and smooth muscle wrapping, which we test experimentally. Our results reveal that transmural pressure signals through RA to balance the relative rates of epithelial growth and smooth muscle differentiation in the developing mouse lung and identify RA as a previously unreported component in the mechanotransduction machinery of embryonic tissues.

KEY WORDS: Mechanosensor, Morphodynamics, Mechanical stress, Computational modeling, Tension

INTRODUCTION

The mammalian lung comprises a branched network of tubes that form a stereotyped tree (Fujii et al., 2020; Metzger et al., 2008). Two morphogenetic motifs build this tree: domain branching of one epithelial tube off the side of another and terminal bifurcation of the tip of an epithelial tube into two daughter branches (Metzger et al., 2008). Domain branching and bifurcation occur concomitantly with stereotyped differentiation of airway smooth muscle (ASM), a contractile tissue that sculpts the proliferating epithelium into new branches in lung explants (Goodwin et al., 2020; Goodwin et al., 2019; Kim et al., 2015). Branching morphogenesis and ASM differentiation are regulated by several soluble signals that form reciprocal feedback loops among the epithelium, mesenchyme and mesothelium, including fibroblast growth factor 10 (Fgf10), Fgf9, sonic hedgehog (Shh), Wnts and bone morphogenetic protein 4 (Bmp4) (Swarr and Morrisey, 2015; Yi et al., 2009). It remains unclear, however, what coordinates the relative rates of epithelial growth and ASM differentiation.

In addition to these biochemical signals, the embryonic lung is exposed to a complex mechanical microenvironment. The developing lung is filled with luminal fluid that is at a higher pressure than the fluid in the pleural cavity, resulting in a positive transmural pressure (ΔP) across the wall of the lung (Harding and Hooper, 1996). Peristaltic contractions of ASM push luminal fluid distally and, during later development, fetal breathing movements further increase ΔP (Harding and Hooper, 1996; Schittny et al., 2000). Clinically, loss of positive ΔP is associated with a decrease in the number of airway branches and pulmonary hypoplasia (Chandrasekharan et al., 2017; Shastry et al., 2012), but the underlying mechanism remains unclear. Using a microfluidic explant system, we recently found that increasing ΔP enhances ASM differentiation and the rate of branching morphogenesis (Nelson et al., 2017).

Here, we used a novel, unbiased RNA-sequencing (RNA-seq) analysis pipeline to identify signaling pathways that are activated by ΔP during lung development. We found that ΔP differentially affects the expression of genes that contain retinoic acid (RA)-response elements (RAREs) in their proximal enhancer regions. We therefore hypothesized that ΔP promotes branching morphogenesis at least in part through RA. Consistently, we found that elevating ΔP increases RA signaling and, through genetic ablation and pharmacological inhibition, that RA signaling is controlled by the mechanosensor Yap. Using predictions from a computational model of the developing airway, we found that RA signaling regulates branching morphogenesis by modulating the relative rates of ASM differentiation and epithelial proliferation. Our results indicate that ΔP signals in part through Yap and RA to regulate lung development.

RESULTS

Bioinformatics analysis uncovers transcription factors that are regulated by ΔP

Using microfluidic chest cavities to apply defined ΔP to embryonic mouse lungs (Fig. 1A), we previously found that airway epithelial branching and ASM differentiation both increase as ΔP increases (Nelson et al., 2017). Here, we carried out bioinformatics analysis on an RNA-seq dataset obtained from lungs held under low (20 Pa) or physiologic (high, 200 Pa) ΔP (Nelson et al., 2017; Olver et al., 2004; Vilos and Liggins, 1982) to identify transcription factors downstream of pressure. Combining the RNA-seq dataset with embryonic day (E)14 lung DNase-hypersensitivity data from the

[1]Department of Molecular Biology, Princeton University, Princeton, NJ 08544, USA. [2]Graduate School of Biomedical Sciences, Rutgers Robert Wood Johnson Medical School, Piscataway, NJ 08854, USA. [3]Lewis-Sigler Institute for Integrative Genomics, Princeton University, Princeton, NJ 08544, USA. [4]Department of Chemical & Biological Engineering, Princeton University, Princeton, NJ 08544, USA. [5]Department of Biosciences, Rice University, Houston, TX 77005, USA. [6]Department of Mechanics and Engineering Science, BIC-ESAT, College of Engineering, Peking University, Beijing 100871, People's Republic of China. [7]Department of Mechanical and Aerospace Engineering, Princeton University, Princeton, NJ 08544, USA. [8]Princeton Institute for the Science & Technology of Materials, Princeton, NJ 08544, USA.

*Author for correspondence (celesten@princeton.edu)

J.M.J., 0000-0001-6145-3378; C.M.N., 0000-0001-9973-8870

Handling Editor: James Briscoe
Received 19 April 2021; Accepted 10 December 2021

Development (2022) 149, dev199726. doi:10.1242/dev.199726

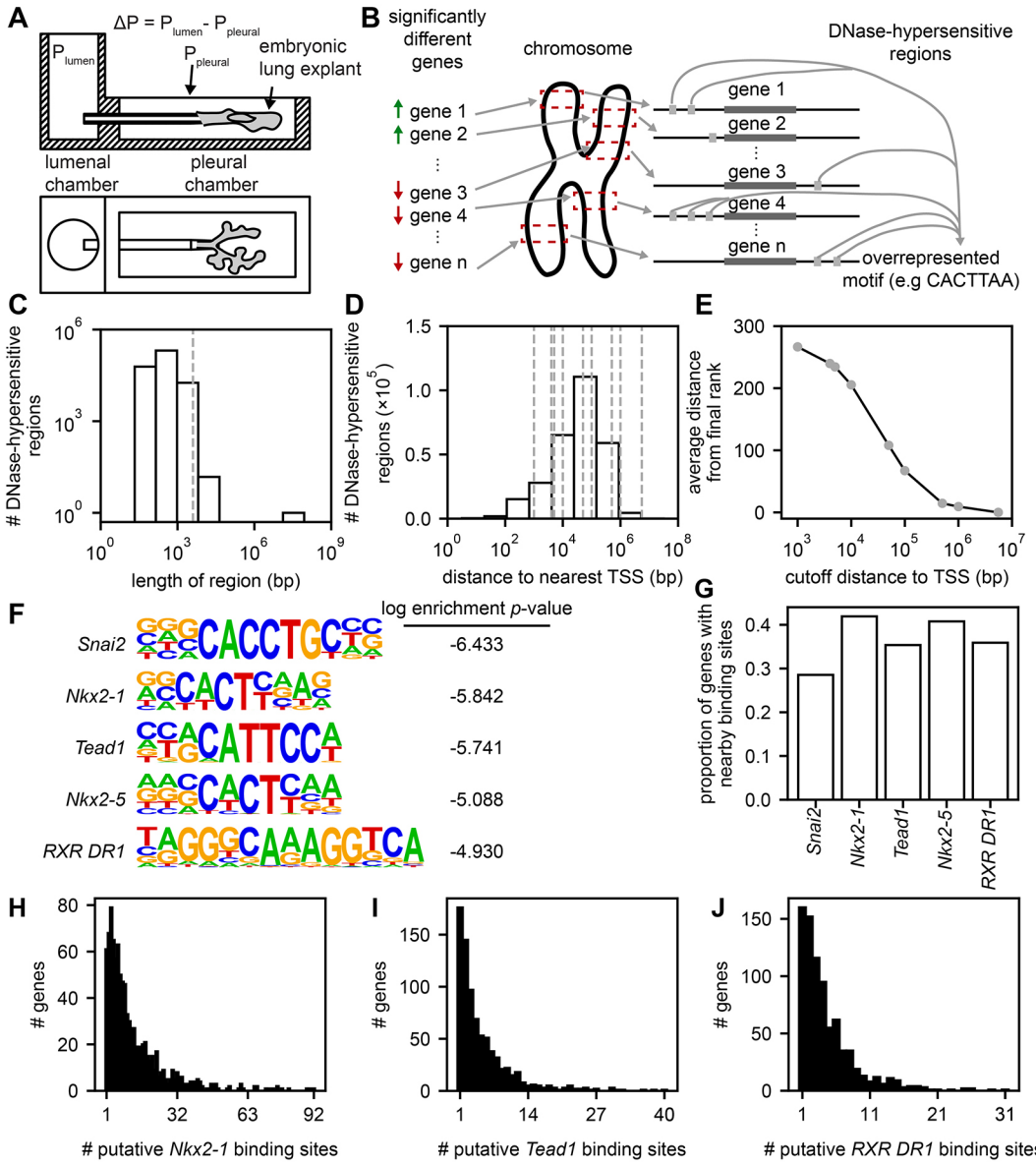

Fig. 1. Bioinformatics approach to identify mechanosensitive transcription factors. (A) Schematic of microfluidic device used to control transmural pressure (ΔP) across embryonic lung explants (Nelson et al., 2017). (B) Workflow for the bioinformatics analysis. (C) Histogram of the lengths of all investigated DNase-hypersensitive regions. Dashed line shows the maximum length included in subsequent analyses. (D) Histogram of the distance of each DNase-hypersensitive region to the nearest TSS in the genome. (E) All identified transcription factor (TF)-binding motifs were ranked by their enrichment *P*-values in DNase-hypersensitive regions within different distances of the TSS in our dataset (corresponding to dashed lines in D). Data points represent the average difference in rank between TFs at each cutoff distance and their rank at the largest cutoff distance. (F) TF-binding motifs that potentially respond to increased ΔP. (G) Proportion of pressure-responsive genes with a specific TF-binding site in a nearby DNase-hypersensitive region. (H-J) The number of genes with a given number of putative binding sites for Nkx2-1 (H), Tead1 (I) and RA receptors (J) in nearby DNase-hypersensitive regions among all pressure-responsive genes.

mouse ENCODE project (Yue et al., 2014) enabled us to identify the DNase-hypersensitive regions near the differentially expressed transcripts. By probing these regions for overrepresented motifs, we uncovered transcription factor-binding sites that are possibly associated with the changes in gene expression induced by ΔP (Fig. 1B; Table S1).

Although the DNase-hypersensitive regions that are closest to a transcription start site (TSS) are those most likely to contain cis-acting elements, important gene-regulatory regions can be located several kilobases away from a TSS (Cheng et al., 2014). We therefore investigated the length of each DNase-hypersensitive region and its distance from a TSS. We found that most DNase-hypersensitive regions were shorter than 4000 base pairs (bp) (Fig. 1C). We examined transcription factor-binding motifs that were significantly overrepresented in DNase-hypersensitive regions within different distances of the TSS in our dataset (Fig. 1D). At each distance cutoff, we ranked each transcription factor by its enrichment *P*-value (Heinz et al., 2010) and calculated the average difference between the rank of a transcription factor and its rank at the largest cutoff, which incorporates the most DNase-hypersensitive regions. As we increased the distance between the TSS and the DNase-hypersensitive regions that we considered, the transcription factors gradually approached their final ranks (Fig. 1E). We also carried out these analyses using DNase-hypersensitivity data from adult mouse lungs and found

Development (2022) 149, dev199726. doi:10.1242/dev.199726

similar distributions of sizes, locations, and convergence upon their final ranks (Fig. S1A-C). We therefore decided to examine the transcription factor-binding motifs identified by including all DNase-hypersensitive regions that are associated with genes differentially expressed in response to ΔP, irrespective of distance from the TSS.

Using this approach, the top-identified motif was a putative binding site for Snai2 (also known as Slug) (Fig. 1F; Fig. S1E), which promotes epithelial-to-mesenchymal transition (EMT) and cell migration (Nieto, 2013). Although Snai2 has not been previously implicated in lung development, EMT plays a role in epithelial repair after lung injury (Vaughan and Chapman, 2013). We also found that Tead1-binding motifs were significantly overrepresented. Tead1 associates with the mechanosensitive transcription factors Yap and Taz (Han et al., 2018; Huraskin et al., 2016); Yap is crucial for proliferation of the lung epithelium during branching morphogenesis (Lin et al., 2017). In our analyses using DNase-hypersensitivity data from both embryonic and adult lungs, we found that putative binding sites for Nkx2-1, Nkx2-5, and retinoic acid receptors (RARs) were overrepresented (Fig. S1D,E). Nkx2-1 regulates airway epithelial progenitors during branching morphogenesis (Herriges and Morrisey, 2014; Wong et al., 2019), whereas Nkx2-5 regulates the differentiation of myofibroblasts and promotes heart development (Chen and Schwartz, 1997; Hu et al., 2010). Several pressure-responsive genes had at least one nearby motif for Snai2 (28.6% of genes), Nkx2-1 (41.9%), Tead1 (35.4%), Nkx2-5 (40.8%) and retinoid X receptor (RXR) DR1 (35.9%) (Fig. 1G). Most genes had one binding site for each transcription factor in their associated DNase-hypersensitive regions; however, for each transcription factor, several genes contained multiple motifs within their associated DNase-hypersensitive regions (Fig. 1H-J). Increasing ΔP therefore activates the expression of genes with binding sites for transcription factors known to be involved in lung development, indicating that pressure may signal through one or more of these pathways.

RA deficiency has been linked to congenital diaphragmatic hernia (CDH) (Keijzer et al., 2000; Major et al., 1998), wherein weaknesses in the developing diaphragm allow abdominal viscera to herniate into the pleural cavity and compress the lung, resulting in pulmonary hypoplasia at birth and respiratory complications throughout life (Montedonico et al., 2008a). RA signaling is thought to modulate ASM differentiation (Chen et al., 2014), which influences airway branching in cultured lung explants (Goodwin et al., 2019; Kim et al., 2015); consistently, ASM is disrupted in rodent models of CDH (Belik et al., 2003; Pederiva et al., 2012). RARγ translocates to the nucleus in response to mechanical signals (Swift et al., 2013). Furthermore, knocking out RARs disrupts cell-matrix adhesion and the actin cytoskeleton, suggesting an important role for this family of receptors in mechanotransduction (Al Tanoury et al., 2014). These observations led us to hypothesize that high ΔP increases the rate of branching morphogenesis in the embryonic lung at least in part by influencing RA signaling. Because our data suggested a previously unrecognized connection between the mechanical environment of the developing lung and RA signaling, we focused our subsequent analysis on this signaling pathway.

RA signaling components are differentially expressed in response to ΔP

Several proteins are involved in the biosynthesis of RA (Fig. 2A). Retinol is transported through the bloodstream in a complex with retinol binding protein 4 (Rbp4; also known as Rbp) and is internalized when this complex binds to its cell-surface receptor, Stra6, or when free retinol, which is lipophilic, diffuses across the plasma membrane (Fernandes-Silva et al., 2020). In the cytoplasm, RA and RA precursors are bound by carrier proteins including cytoplasmic retinol-binding protein 1 (Crbp1; Rbp1) and cytoplasmic RA-binding proteins 1 and 2 (Crabp1/2). Retinol is oxidized to retinal, which is then further oxidized to RA by aldehyde dehydrogenase 1,2,3 (Aldha1/2/3; Raldh1/2/3). RA binds RAR/RXR dimers at RAREs to activate transcription of target genes. Retinal can also be stored through processing by lecithin retinol acyltransferase (Lrat) and RA is degraded by Cyp26b1.

The expression of *Adh1*, *Rbp1* and *Aldh1a1*, genes that synthesize or bind to and stabilize RA intermediates, was significantly increased under high ΔP (Fig. 2B-D; Fig. S2A). Expression of *Rdh14*, which synthesizes retinal, and *Crabp1*, however, were both significantly decreased. Expression of *Cyp26b1* was also significantly decreased. Overall, these data are consistent with increased production and decreased degradation of RA, which would lead to an increase in RA levels, concordant with our DNase-hypersensitivity analysis suggesting increased RA signaling under high ΔP.

Expression of RA signaling components in different compartments of the lung

To define the tissue compartments that express the RA-biosynthetic machinery, we combined *in situ* hybridization with single-cell RNA-sequencing (scRNA-seq) analysis of E11.5 lungs. As expected, both approaches revealed that *Nkx2-1* is expressed in the airway epithelium (Fig. 3A,B; Fig. S3A). We found that *Rara* is expressed in all tissues of the lung, most prominently in the mesenchyme and mesothelium (Fig. 3C,D; Fig. S3B) and that *Rarb* is expressed in the mesenchyme and mesothelium but is most strongly expressed in the trachea and proximal airway epithelium (Fig. 3E,F; Fig. S3C). Our scRNA-seq data do not show epithelial expression of *Rarb*, likely because the tissue used for sequencing excluded the trachea and proximal bronchi where the *Rarb* probes most strongly hybridize. Consistently, scRNA-seq data from E15 lungs show that the levels of *Rarb* are higher in *Sox2*-expressing proximal epithelial cells than in *Sox9*-expressing distal epithelial cells (Fig. S3D). We found that *Aldh1a2* is expressed primarily in the mesothelium (Fig. 3G,H; Fig. S3E-G). *Rbp1* is expressed in all lung tissues (Fig. 3I). *Stra6* is expressed in the mesenchyme and in a large proportion of ASM (Fig. 3J). The fact that these genes are expressed at this early stage of development is consistent with previous findings (Malpel et al., 2000) and with a possible role for RA downstream of ΔP in the developing lung.

ΔP enhances RA signaling in the early embryonic mouse lung

To test directly whether pressure activates RA signaling, we isolated lungs from E11.5 mouse embryos that express *lacZ* under the control of the RARE from the *Rarb* promoter (*RARE-lacZ*), which reports RA signaling (Rossant et al., 1991), and cultured the explants in the presence of the adenylate cyclase agonist forskolin (Seamon et al., 1981). Forskolin promotes chloride and fluid secretion out of airway epithelial cells into the lumen of the lung (Dekkers et al., 2013), which increases ΔP and physically expands the airway (Fig. 4A). We found that treatment with forskolin increases β-galactosidase activity in *RARE-lacZ* lung explants (Fig. 4B; Fig. S4A), consistent with our bioinformatics analysis implicating RA downstream of high ΔP. Curiously, histological sections revealed that, although lung explants treated with vehicle control express β-galactosidase primarily in the mesenchyme, those cultured in the presence of forskolin show an increase in β-galactosidase specifically in the epithelium (Fig. 4C,D), without

Development (2022) 149, dev199726. doi:10.1242/dev.199726

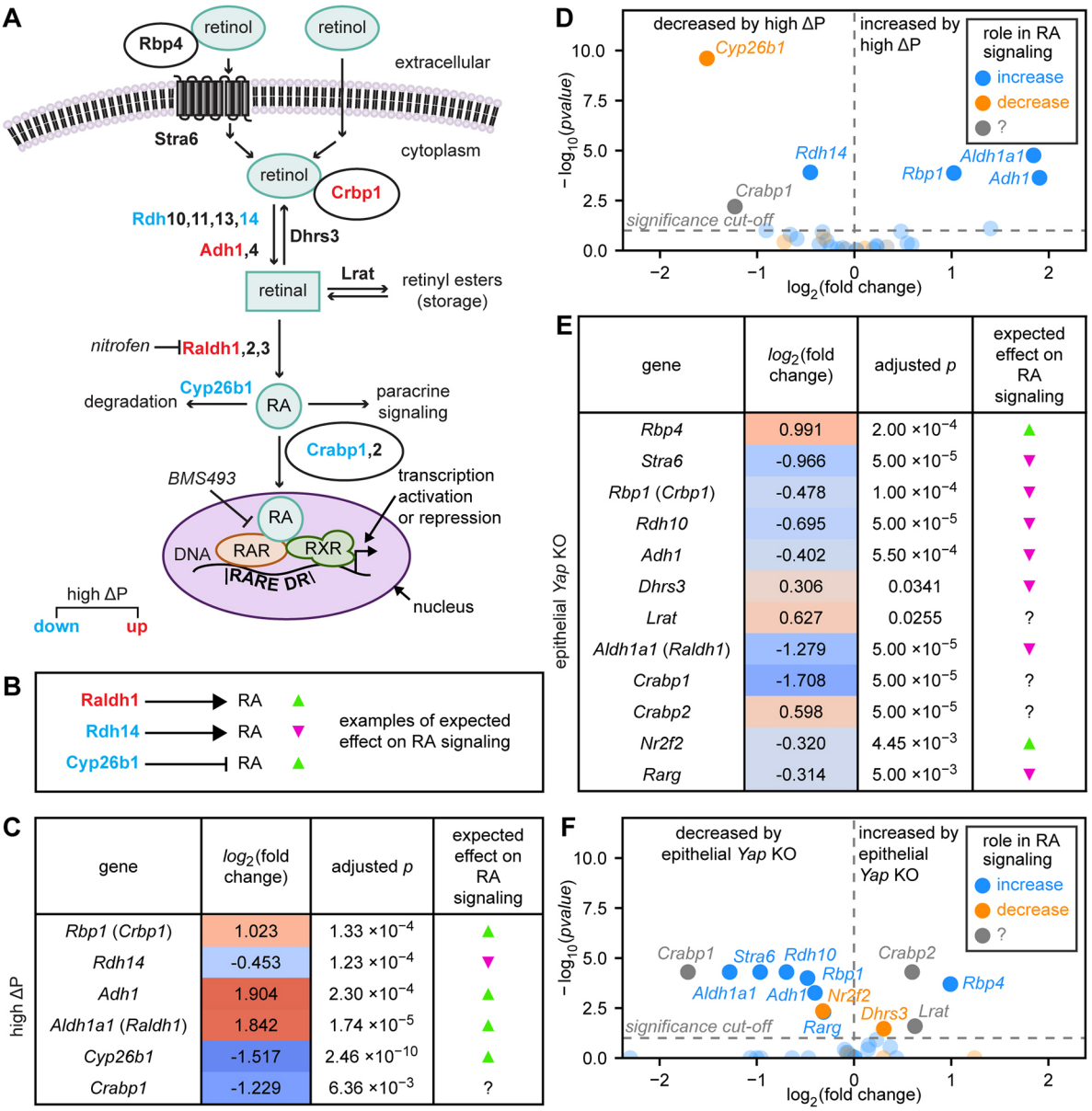

Fig. 2. Expression of genes in the RA-biosynthetic pathway is modulated by ΔP. (A) Schematic of the RA biosynthetic pathway, inspired by Fernandes-Silva et al. (2020). Under high ΔP, genes shown in blue decrease expression whereas those shown in red increase expression. (B) Examples of how the expected effect on RA signaling is determined. (C,E) Relative expression, adjusted *P*-value, and expected effect on RA signaling of genes in the RA-biosynthetic pathway that are significantly differentially expressed in the lung under high ΔP (C) or when *Yap* is conditionally knocked out of the airway epithelium (E). (D,F) Volcano plots of the gene expression changes from panel C (solid dots) and Fig. S2A (translucent dots) (D) and from panel E (solid) and Fig. S2B (translucent) (F).

affecting epithelial proliferation (Fig. 4E,F). Increasing ΔP therefore enhances RA signaling in the epithelium of lung explants.

We previously found that high ΔP leads to increased ASM differentiation and epithelial bifurcations (Kim et al., 2015; Nelson et al., 2017). Consistently, immunofluorescence and qPCR analysis revealed that treatment with forskolin maintains the differentiation of ASM at sites of epithelial bifurcation (Fig. 4G; Fig. S4B). To quantify the spatial pattern of ASM differentiation, we correlated α-smooth muscle actin (αSMA) staining intensity with epithelial curvature around distal lung branches and found there was no difference between lungs treated with forskolin and controls (Fig. 4G,H). These data suggest that culture under high ΔP maintains ASM differentiation and allows continued sculpting of the epithelium into bifurcations.

We next sought to define the mechanism by which pressure promotes RA signaling in the developing lung. RARs could be directly mechanosensitive, for example by translocating to the nucleus in response to force. Alternatively, RA signaling could be downstream of another mechanosensor, such as Yap, which associates with Teads to induce transcription in response to mechanical force (Liu-Chittenden et al., 2012). Yap has been implicated in RA signaling in the adult lung epithelium (Ng-Blichfeldt et al., 2018) and in other systems (Mezquita et al., 2018; Xiao et al., 2018). Based on our findings that Tead1-binding motifs are over-represented in cis-regulatory elements of pressure-responsive genes (Fig. 1F), we hypothesized that ΔP signals through Yap to increase the expression of the RA-biosynthetic machinery. Consistent with this hypothesis, we found that increasing ΔP by culturing lungs

Development (2022) 149, dev199726. doi:10.1242/dev.199726

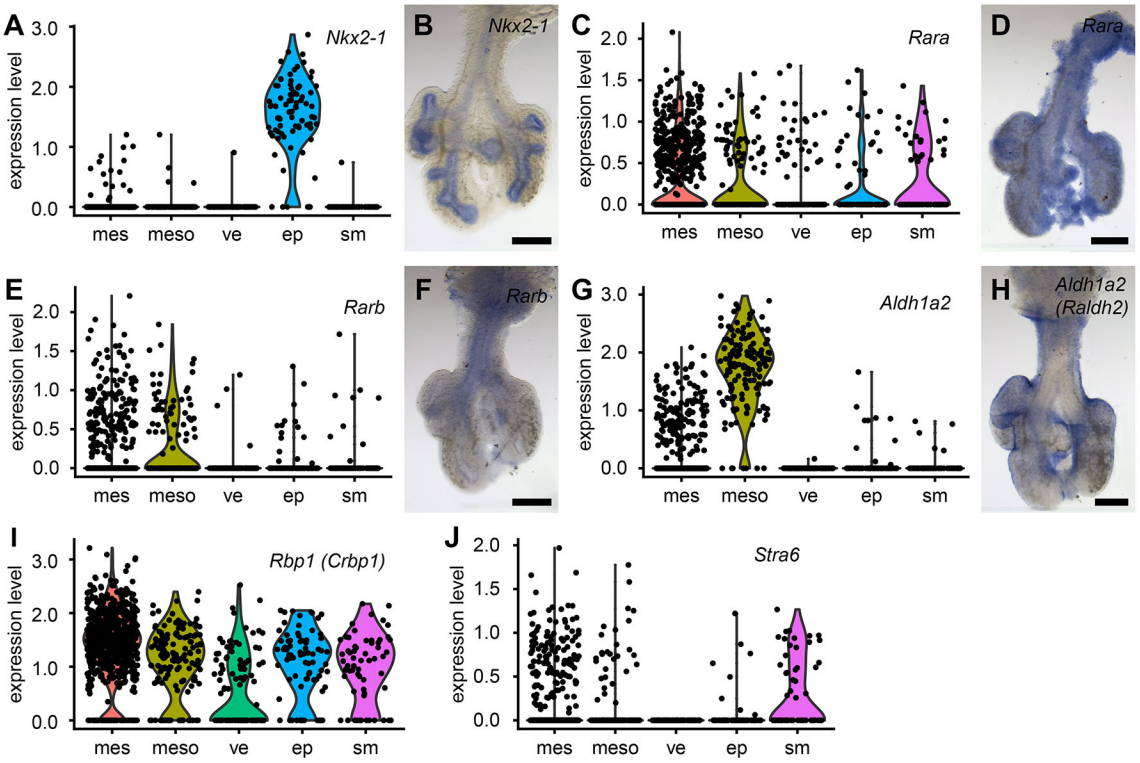

Fig. 3. Lung expression patterns of *Nkx2-1* and genes in the RA-biosynthetic pathway. (A-J) Shown are scRNA-seq analysis and *in situ* hybridization for *Nkx2-1* (A,B), *Rara* (C,D), *Rarb* (E,F), *Aldh1a2* (G,H), *Rbp1* (I) and *Stra6* (J). Violin plots show distributions of normalized and scaled counts of gene expression in the cell population. Dots represent individual cells. Scale bars: 250 µm. ep, epithelium; mes, mesenchyme; meso, mesothelium; sm, smooth muscle; ve, vascular endothelium.

in the presence of forskolin induces nuclear localization of Yap in the epithelium (Fig. 4I,J). To determine whether Yap is upstream of the RA-biosynthetic machinery, we evaluated a published RNA-seq dataset acquired from *Shh-Cre;Yap*$^{fl/fl}$ (epithelial *Yap* KO) lungs and littermate controls (Lin et al., 2017). This dataset revealed that epithelial knockout of *Yap* leads to a significant decrease in the expression of *Rbp1*, *Adh1*, *Aldh1a1* and *Crabp1*, among other genes in the RA-biosynthetic pathway (Fig. 2E,F; Fig. S2B), consistent with our hypothesis that pressure signals through Yap to induce RA signaling.

To investigate directly whether Yap signals to RA, we cultured *RARE-lacZ* lung explants in the presence of verteporfin, which blocks Yap-Tead interactions and Yap-dependent gene expression (Liu-Chittenden et al., 2012). As predicted, we found that verteporfin reduces nuclear localization of Yap (Fig. S4C,D) and decreases X-gal staining in *RARE-lacZ* lung explants (Fig. 4K,L; Fig. S4E) without increasing apoptosis (Fig. S4C). To disrupt Yap specifically in the epithelium, we generated *RARE-lacZ* embryos in which we conditionally deleted Yap from the airway epithelium (*Shh-Cre;Yap*$^{fl/fl}$*;RARE-lacZ*). Consistent with our verteporfin experiments, *Shh-Cre;Yap*$^{fl/fl}$*;RARE-lacZ* lungs showed significantly decreased X-gal stain within the epithelium compared with littermate controls, both in histological sections (Fig. 4M,N; Fig. S4F) and in epithelial rudiments denuded of mesenchyme (Fig. S4G). RA signaling is therefore downstream of Yap in the developing lung.

Inhibiting RA decreases epithelial branching and ASM wrapping in lung explants

Given that high ΔP increases both RA signaling and epithelial branching, we hypothesized that RA promotes morphogenesis of the embryonic lung. First, we confirmed that retinoids in the culture medium would not interfere with our ability to detect changes in branching in lung explants (Fig. S5A,B). Next, we inhibited RA signaling by culturing E11.5 lung explants in the presence of the pan-RAR inverse agonist BMS493 (Chen et al., 2014), which decreased β-galactosidase activity in *RARE-lacZ* reporter lungs (Fig. S5C-H) and reduced expression of the RA pathway target *Rarb* (Fig. 5A), but did not affect Yap nuclear localization in the epithelium (Fig. S5I,J). We found that explants treated with BMS493 develop dilated airways (Fig. 5B) and form fewer branches (Fig. 5C) than those treated with vehicle control, indicating that RA signaling promotes airway branching. Consistently, treatment with BMS493 also decreases branching in lungs cultured under high ΔP (Fig. S5K,L). Aberrant RA signaling has been linked to CDH (Beurskens et al., 2007) and the nitrofen rodent model of CDH acts, at least in part, by disrupting RA biosynthesis (Chinoy et al., 2001; Mey et al., 2003; Nakazawa et al., 2007). The underdeveloped lungs of the nitrofen model are thought to result from a combination of direct and indirect effects on the lung, the latter through malformation of the diaphragm (Keijzer et al., 2000). Consistently, we found that explants cultured in the presence of nitrofen form fewer, more dilated branches than those cultured with vehicle control (Fig. 5D,E), confirming that nitrofen can directly affect lung branching independently of its effects on the diaphragm (Chinoy et al., 2001). RA signaling therefore promotes branching in lung explants.

We previously found that altering the rate of epithelial proliferation significantly alters the pattern of branching in mesenchyme-free lung explants (Varner et al., 2015). We therefore asked whether RA signaling affects branching by tuning epithelial proliferation. We found that exposure to BMS493 does

Development (2022) 149, dev199726. doi:10.1242/dev.199726

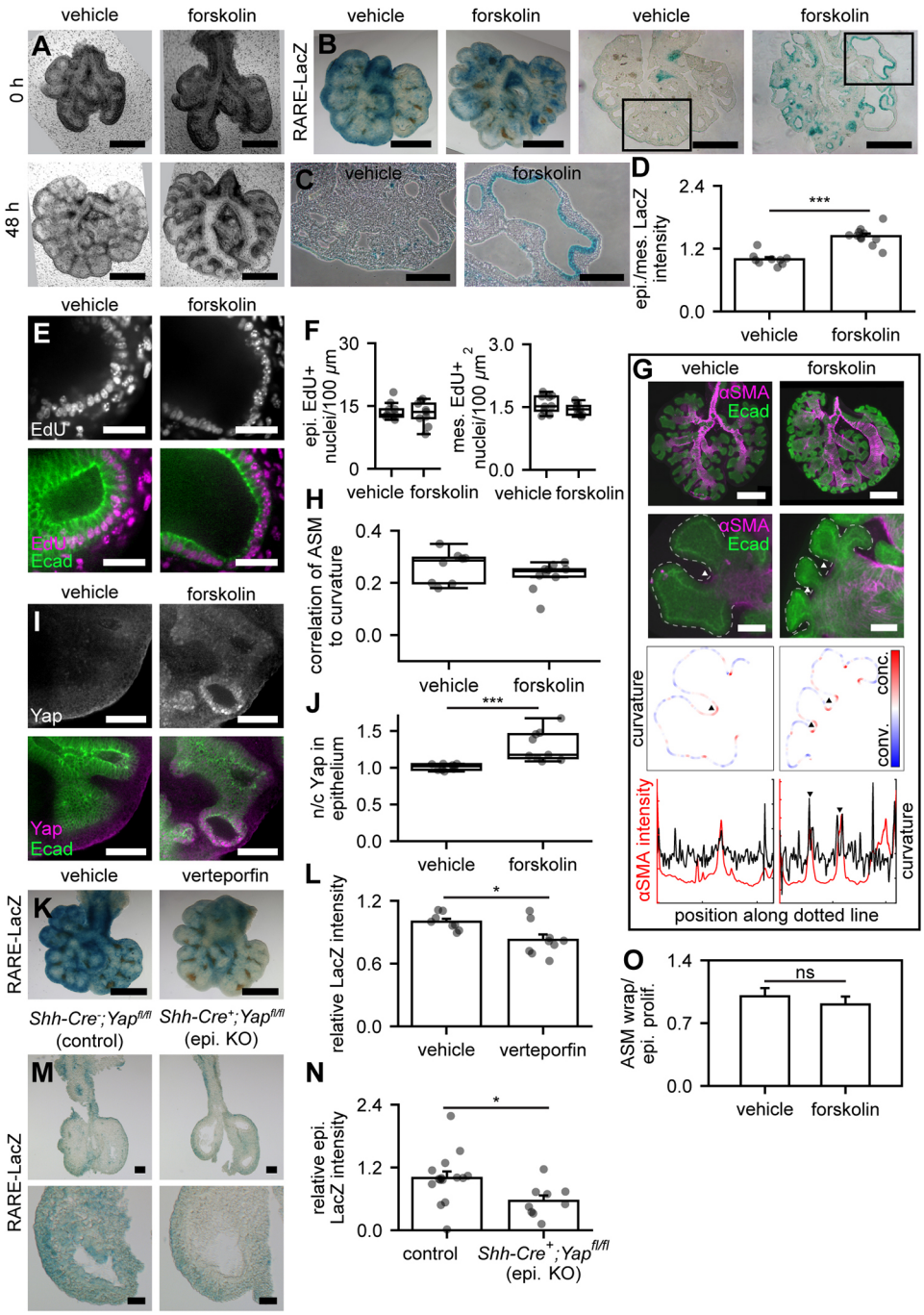

Fig. 4. RA signaling is downstream of ΔP and Yap. (A-D) Brightfield images (A), X-gal staining in wholemounts or sections (B,C) and quantification of X-gal staining (D) in E11.5 lungs explanted from *RARE-lacZ* reporter mice cultured in the presence of forskolin or vehicle control (DMSO) for 48 h. $P=3.36\times10^{-6}$ by unpaired, two-tailed Student's *t*-test. (E-H,O) Immunofluorescence analysis for Ecad and EdU (E), quantification of relative proliferation of distal branches (F), immunofluorescence analysis for αSMA and Ecad (G), quantification of the correlation of αSMA staining intensity to epithelial curvature (H), and ratio of smooth muscle wrapping to epithelial proliferation (O) in E11.5 lung explants cultured in the presence of forskolin or vehicle control for 48 h. (I,J) Immunofluorescence analysis for Yap and Ecad (I) and quantification of the ratio of nuclear to cytoplasmic Yap (J) in the epithelium of lungs cultured in the presence of forskolin or vehicle control for 48 h. ***$P=9.64\times10^{-4}$ by unpaired, two-tailed Student's *t*-test. (K,L) X-gal staining (K) and quantification of total X-gal staining (L) of E11.5 lungs explanted from *RARE-lacZ* reporter mice cultured in the presence of verteporfin or vehicle control for 24 h. *$P=0.0124$ by unpaired, two-tailed Student's *t*-test. (M,N) X-gal staining (M) and quantification of epithelial X-gal staining (N) in E11.5 *Shh-Cre;Yap$^{fl/fl}$;RARE-lacZ* reporter lung sections and epithelial rudiments or littermate controls; five independent experiments. *$P=0.0238$ by unpaired, two-tailed Student's *t*-test. Bar graphs represent mean+s.e.m. In box-and-whisker plots, the midline, box, and whiskers represent the median, upper and lower quartiles, and furthest points, respectively, with the whiskers excluding outliers defined as points further than 1.5× interquartile range outside of the box limits. conc., concave; conv., convex; epi., epithelial; KO, knockout; mes., mesenchymal; n/c, nuclear to cytoplasmic ratio; ns, not significant. Scale bars: 500 µm (A,B,K); 200 µm (C); 25 µm (E); 250 µm (G, first row); 50 µm (G, second row, I,M, bottom row); 100 µm (M, top row).

not significantly affect 5-ethynyl-2′-deoxyuridine (EdU) incorporation in the epithelium in lung explants (Fig. 5F,G), suggesting that RA signaling promotes the formation of branches without altering epithelial proliferation.

Branching is influenced by patterned differentiation of ASM (Goodwin et al., 2019; Kim et al., 2015) and deposition of fibronectin (Sakai et al., 2003) around the airway epithelium in cultured lung explants. We therefore sought to determine whether RA signaling is necessary for ASM differentiation or fibronectin localization around developing epithelial branches. Immunofluorescence staining showed that treatment with BMS493 led to a reduction in ASM localizing to sites of epithelial bifurcation (Fig. 5H,I) but did not affect the distribution of fibronectin around epithelial branches (Fig. S5M,N). Instead, inhibiting RA signaling induced the formation of dilated and buckled epithelium lacking ASM. We therefore hypothesized that inhibiting RA signaling reduces epithelial branching in part by decreasing ASM differentiation. Consistent with this hypothesis, qRT-PCR analysis of E11.5 lung explants cultured in the presence of BMS493 revealed a significant reduction in the expression of αSMA (*Acta2*), which is a marker of contractile smooth muscle cells (Jaslove and Nelson, 2018), transgelin (*Tagln*; SM22α) (Li et al., 1996; Liu et al., 2017) and calponin (*Cnn1*). In contrast, the level of serum response factor (*Srf*), the main regulator of ASM differentiation, is not significantly affected by treatment with BMS493 (Fig. 5A), suggesting that RA signaling is required for the differentiation of ASM independently of Srf.

Physical stretch induces embryonic lung mesenchymal cells to elongate and differentiate into ASM in culture (Yang et al., 2000).

Development (2022) 149, dev199726. doi:10.1242/dev.199726

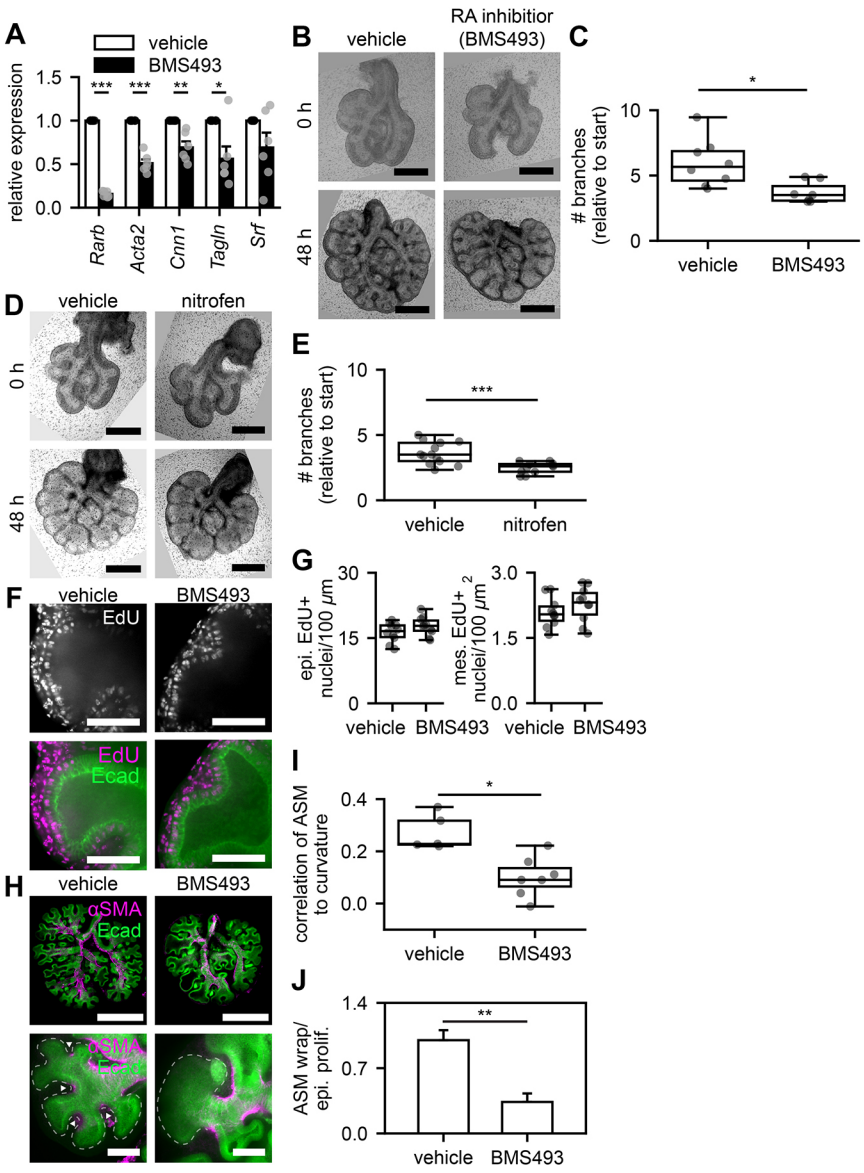

Fig. 5. Inhibiting RA decreases branching and ASM wrapping in lung explants. (A) qRT-PCR analysis of *Rarb* and ASM markers in lung explants cultured in the presence of BMS493 or vehicle control (DMSO) for 48 h. *P*-values per unpaired, two-tailed Student's *t*-test: *Rarb*, 2.40×10^{-14}; *Acta2*, 5.15×10^{-7}; *Cnn1*, 0.0111; *Tagln*, 0.00117. Data points represent pooled RNA from two/three lungs from six independent experiments. (B-E) Brightfield images (B,D) and quantification (C,E) of the number of epithelial branches in E11.5 lung explants treated with BMS493 (B,C) or nitrofen (D,E) or vehicle control for 48 h. *P*-values per unpaired, two-tailed Student's *t*-test: BMS493, 0.0100; nitrofen, 0.000581. (F-J) Immunofluorescence analysis for Ecad and EdU (F) and quantification of the density of EdU^+ epithelial or mesenchymal cells (G), immunofluorescence analysis for αSMA and Ecad (H), quantification of the correlation of αSMA staining intensity to epithelial curvature (I; **P*=0.00241 by unpaired, two-tailed Student's *t*-test) and ratio of ASM wrapping to epithelial proliferation (J; ***P*=0.00230 by a permutation test) in E11.5 lung explants cultured in the presence of BMS493 or vehicle control for 48 h. Data are mean+s.e.m. In box-and-whisker plots, the midline, box, and whiskers represent the median, upper and lower quartiles, and furthest points, respectively, with the whiskers excluding outliers defined as points further than 1.5× interquartile range outside of the box limits. Scale bars: 50 µm (F,H, bottom row); 500 µm (B,D,H, top row).

We therefore cultured primary embryonic lung mesenchymal cells on microcontact-printed squares or lines of fibronectin to vary cell elongation and thus mimic the morphologies observed before and after application of mechanical strain (George et al., 2015; Yang et al., 2000). We found that elongated cells develop αSMA-containing fibers along their long axes (Fig. S6A,B), which is characteristic of contractile smooth muscle (Jaslove and Nelson, 2018), and express higher levels of αSMA protein than rounded cells (Fig. S6C,D), consistent with previous reports (Yang et al., 1999). Surprisingly, we found that blocking RA signaling does not affect the expression of αSMA (Fig. S6E). These data suggest that, in the intact lung, RA signaling indirectly promotes ASM differentiation in a non-cell-autonomous manner. This conclusion is consistent with our observation that increasing ΔP enhances RA signaling specifically within the epithelium.

A computational model predicts that ASM wrapping induces epithelial branching in response to pressure

To determine whether a decrease in ASM wrapping can explain the dilated epithelial morphologies we observe when RA is inhibited, we used the finite element method (FEM) to solve a mechanical model of the developing airway. We modeled the lung as three layers of tissue: the epithelium, ASM, and undifferentiated mesenchyme (Fig. 6A,B; Fig. S7A-C), using measurements of epithelial and mesenchymal thicknesses from confocal slices of E11.5 lungs and published estimates of the relative stiffnesses of these tissues (Alcaraz et al., 2003; Chevalier et al., 2016; Smith et al., 2005) (Fig. 6C). We accounted for tonic ASM contractions at this developmental stage (Jaslove and Nelson, 2018) by modeling this tissue as the stiffest of the three layers. As a first approximation, we assumed that the epithelium grows isotropically in the tangential plane to the tissue at every point. Viscoelastic relaxation of embryonic tissue occurs over minutes (Chevalier et al., 2016), whereas epithelial branches form over 12-24 h (Fig. 4A). Therefore, the rate of tissue growth is slow relative to the rate of mechanical relaxation, and we assumed that the tissue is in quasi-static equilibrium at each time point (Goodwin et al., 2019). Finally, to make the model computationally tractable, we used this quasi-static assumption to approximate all three tissue layers as hyperelastic materials.

Development (2022) 149, dev199726. doi:10.1242/dev.199726

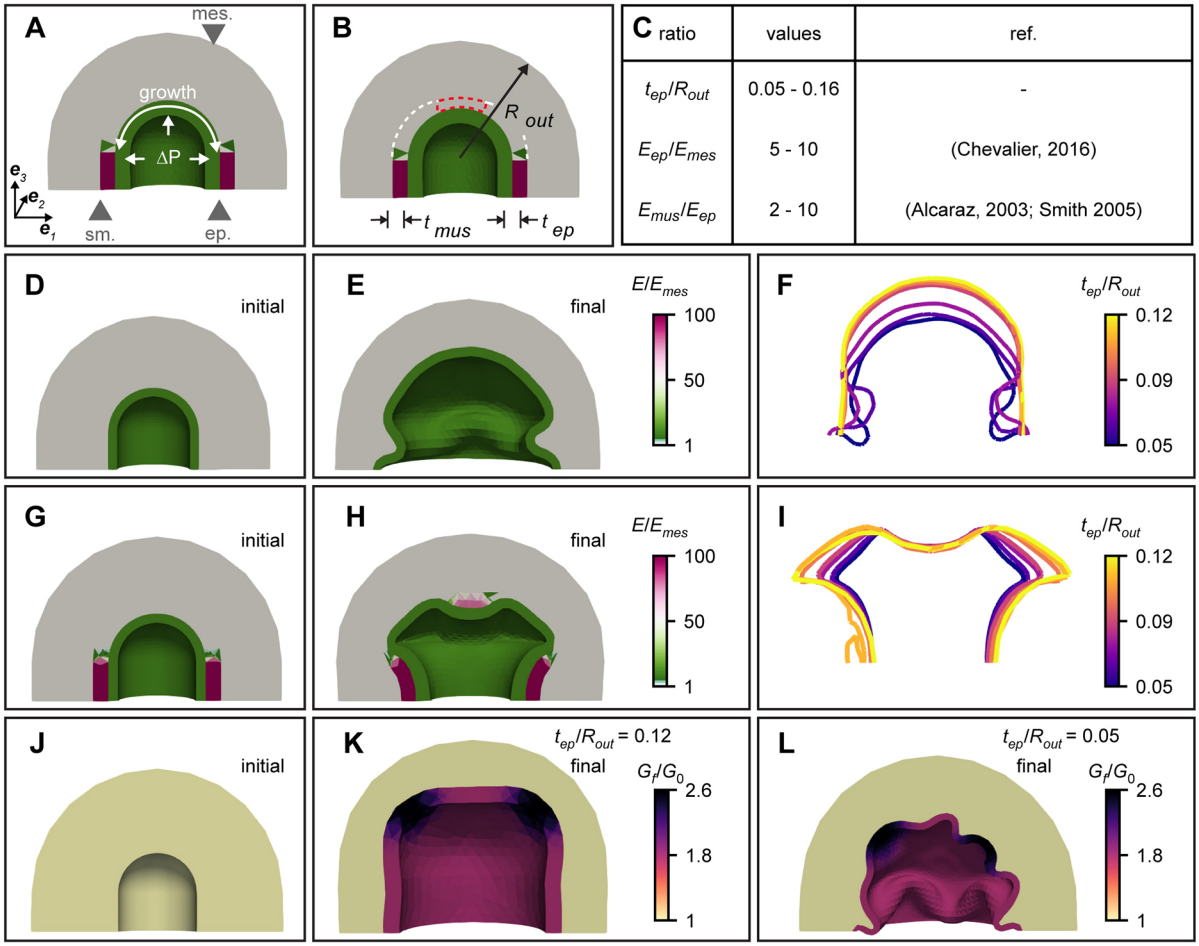

Fig. 6. Computational model reveals that ASM wrapping promotes epithelial branching. (A,B) Schematic of the geometry of the model and the corresponding tissue layers. In B, dashed red box denotes region of ASM differentiation during the simulation time and dashed white line indicates that the thickness of the ASM layer is the same at all locations. (C) Ratios of key parameters used in the model. (D,G,J) Initial geometries of simulations with no ASM (D), ASM wrapping around the epithelium (G) or increased proliferation along the flanks of the epithelium (J). (E,H,K) Final geometries of simulations in panels D, G or J, respectively. (F,I) Final geometries of simulations using different epithelial thicknesses for the classes of models represented by panels D or G, respectively. (L) Final geometry of the simulation in panel J with t_{ep}/R_{out}=0.05. Colors in panels D, E, G and H represent stiffness. Colors in panels J, K and L represent the final volume of the tissue at each location.

In the absence of ASM, our simulations revealed that the epithelium dilates and eventually buckles (Fig. 6D,E; Movie 1). Given that the thickness of the airway epithelium relative to its surrounding mesenchyme can vary (Fig. 6C), we explored the parameter space of our models by changing the relative thickness of the epithelial layer. We found that epithelia of all thicknesses dilate in the absence of ASM, but that decreasing the relative thickness of the epithelium (t_{ep}/R_{out}) leads to more buckling (Fig. 6F). We next used the computational model to define the effects of ASM wrapping on the geometry of the epithelium and found that the presence of ASM is sufficient to induce bifurcations (Fig. 6G,H; Movie 2), regardless of epithelial thickness (Fig. 6I). The dilated and buckled geometries of models without ASM (Fig. 6E,F) are reminiscent of the epithelia that we observed in explants cultured in the presence of RA inhibitors (Fig. 5H). In contrast, the bifurcated geometries we observed in models with ASM (Fig. 6H,I) are similar to the bifurcated branches in lungs cultured in control conditions (Fig. 5H), supporting our conclusion that the dilated, buckled epithelial morphology observed in explants treated with RA inhibitors results from losses of ASM wrapping. Loss of *Yap* decreases actomyosin contractility and mechanical tension in the developing lung epithelium (Lin et al., 2017). To determine whether changes in epithelial mechanics could account for the observed effects on lung branching, we varied the stiffness of the epithelial layer in our model and found that the overall geometry of the branches is defined by smooth muscle wrapping regardless of epithelial stiffness (Fig. S7D-I). The similarities between our computational and experimental results suggest that our approximation of the three tissue layers as hyperelastic materials captures the most salient aspects of branch initiation.

An alternative (but not mutually exclusive) hypothesis is that localized increases in epithelial proliferation lead to epithelial outgrowth and terminal bifurcation (Varner and Nelson, 2014). Using our computational model, we found that patterned increases in epithelial proliferation lead to flattening of the epithelium, reminiscent of the early stages of bifurcation (Kim et al., 2015), but are not sufficient to generate bifurcations in the absence of ASM (Fig. 6J,K; Movie 3). In addition, this flattened morphology depends on the relative thickness of the epithelium: when epithelial thickness is set near the low end of our experimentally measured range, the entire structure buckles (Fig. 6L; Movie 4). Our simulations therefore suggest that robust bifurcations require an external mechanical constraint, such as that from ASM differentiation.

Development (2022) 149, dev199726. doi:10.1242/dev.199726

A computational model predicts that the relative rates of ASM differentiation and epithelial proliferation determine epithelial morphology

The results of our simulations led us to hypothesize that the rate of ASM differentiation relative to that of epithelial growth (proliferation) is a key parameter for determining whether the lung branches or dilates. We experimentally tested this hypothesis by performing EdU analysis on lungs treated with forskolin or BMS493 and comparing the amounts of ASM localizing to sites of bifurcation to the rates of epithelial proliferation. We found that inhibiting RA signaling decreases ASM wrapping relative to epithelial proliferation (Fig. 5J) and leads to dilated epithelial branches. In contrast, increasing ΔP by culturing with forskolin maintains the balance between ASM wrapping and epithelial proliferation (Fig. 4O), resulting in normal branch morphology.

We therefore investigated the effect of changing these relative rates in the computational model. Our results revealed that decreasing the rate of ASM differentiation relative to epithelial proliferation promotes the formation of a dilated tissue; conversely, increasing the rate of ASM differentiation relative to epithelial proliferation promotes bifurcation (Fig. 7A-C). These simulations predicted that inducing proliferation specifically in the epithelium would also lead to a dilated morphology. To test this prediction experimentally, we cultured E11.5 lung explants in the presence of exogenous Fgf1 to promote epithelial proliferation (Varner et al., 2015; Wang et al., 2005) (Fig. 7D,E), which caused the lungs to form fewer branches (Fig. 7F,G) that lack ASM wrapping (Fig. 7H,I). As predicted, inducing the epithelium to proliferate faster than the ASM differentiates (Fig. 7J) led to dilated epithelial branches.

By E12, *Shh-Cre;Yap*$^{fl/fl}$ lungs form dilated epithelial cysts instead of branches (Fig. 7K) (Isago et al., 2020; Lin et al., 2017). We found that epithelial deletion of Yap results in decreased RA signaling in the epithelium and decreased expression of ASM markers and epithelial signals that promote ASM differentiation, including *Shh*, *Tgfb2* and *Tgfb3* (Fig. S8A,B). We therefore hypothesized that the failure of these lungs to form branches was due, at least in part, to a decrease in the rate of ASM differentiation relative to epithelial proliferation. EdU analysis revealed that epithelial deletion of Yap had no effect on epithelial proliferation (Fig. 7L,M), but decreased the correlation between epithelial curvature and αSMA staining intensity (Fig. 7N) relative to controls. Overall, ASM wrapping relative to epithelial proliferation is greatly decreased in *Shh-Cre;Yap*$^{fl/fl}$ lungs (Fig. 7O) and is not rescued by treating explants with forskolin to increase ΔP (Fig. 7P; Fig. S8C). The severe branching defects observed in these lungs is consistent with decreased mechanical constraint on the epithelium from ASM downstream of reduced RA signaling. Altogether, these data reveal that ΔP signals through Yap to activate RA in the epithelium, which increases ASM differentiation and promotes epithelial branching.

DISCUSSION

Here, we describe an unbiased approach that combines publicly available information about genome-wide regulatory regions with RNA-seq analysis to uncover novel transcriptional regulators of morphogenesis. We used data on chromatin accessibility as a proxy for enhancer regions. As the ENCODE project approaches its goal of acquiring ChIP-seq data for every known transcription factor and provides other measures of chromatin accessibility such as ATAC-seq in a wide array of tissues and at more developmental time points (Encode Project Consortium et al., 2020; He et al., 2020), investigations based on our approach will be able to uncover signaling pathways involved in specific developmental events with more precision and fewer false-positives.

Consensus motifs for Nkx2-1 are overrepresented in DNase-hypersensitive regions near genes increased under high ΔP in the lung, which is expected given that *Nkx2-1* is expressed throughout the epithelium during lung development (Herriges and Morrisey, 2014) and that high ΔP increases expression of *Nxk2-1* (Nelson et al., 2017). Although we also identified consensus motifs for Nkx2-5, this is likely a false-positive result due to the similarity between its motif and that of Nkx2-1 and the lack of a known role for Nkx2-5 in lung development. Our top identified motif was for Snai2. Snai2 is a transcription factor expressed by migratory cells during gastrulation and development of the neural crest (Mayor et al., 1995; Nieto et al., 1994), and was previously found to be expressed in the mesenchyme of the developing mouse lung (Savagner et al., 1998). Although Snai2 has not been previously implicated in lung development, we speculate that this transcription factor is involved in mesenchymal motility or remodeling during branching morphogenesis. Unexpectedly, we found that binding sites for RARs and Tead1 are also overrepresented in DNase-hypersensitive regions near pressure-responsive genes. The results of our analysis support a model in which high ΔP activates Yap to increase RA signaling in the developing lung (Fig. 8A,B). Our data show that pressure enhances RA signaling in the epithelium and tunes the relative rates of ASM differentiation and epithelial proliferation to promote branching (Fig. 8C). Conditions that disrupt this balance lead to decreased branching and a dilated or buckled epithelial morphology (Fig. 8D).

Dysregulated RA signaling is thought to contribute to weakening of the diaphragm during development in humans (Loo et al., 2018), rats (Montedonico et al., 2006, 2008b; Nakazawa et al., 2007) and mice (Clugston et al., 2010; Nakamura et al., 2020). Diaphragmatic weakening permits herniation of the abdominal viscera and compression of the lung. Previous investigations have also suggested that decreased RA signaling directly decreases airway branching (Chinoy et al., 2001; Keijzer et al., 2000). Our data show that high ΔP enhances the expression of the RA-biosynthetic machinery and induces RA signaling in the developing lung. These data suggest that diaphragmatic herniation and consequent compression of the lungs cause decreased RA biosynthesis within the developing lung tissues themselves, potentially in a positive-feedback loop that worsens defects in pulmonary morphogenesis in the context of CDH. Future studies are needed to define the mechanical signaling pathways, including those involving Yap, that are altered during lung hypoplasia secondary to CDH.

RA serves several functions in the lung – inducing the primary lung bud (Chen et al., 2010, 2007), stimulating proliferation of the mesenchyme (Schuger et al., 1993), shifting alveolar epithelial differentiation from type I towards type II cells (Wongtrakool et al., 2003) and maintaining ASM homeostasis later in life (Chen et al., 2018). Nonetheless, the precise role of RA signaling during airway branching is controversial: some authors report that treatment with exogenous RA up to a maximum dose increases branching in lung explants (Fernandes-Silva et al., 2020; Pereira-Terra et al., 2015; Schuger et al., 1993), whereas others using higher concentrations of RA or longer durations of exposure have concluded that RA decreases branching (Cardoso et al., 1995; Chazaud et al., 2003; Malpel et al., 2000; Mollard et al., 2000). Our finding that RA signaling balances the relative rates of ASM differentiation and epithelial proliferation provides a possible explanation for these apparently contradictory results: either increasing or decreasing RA signaling has the potential to disrupt this balance and lead to a

Development (2022) 149, dev199726. doi:10.1242/dev.199726

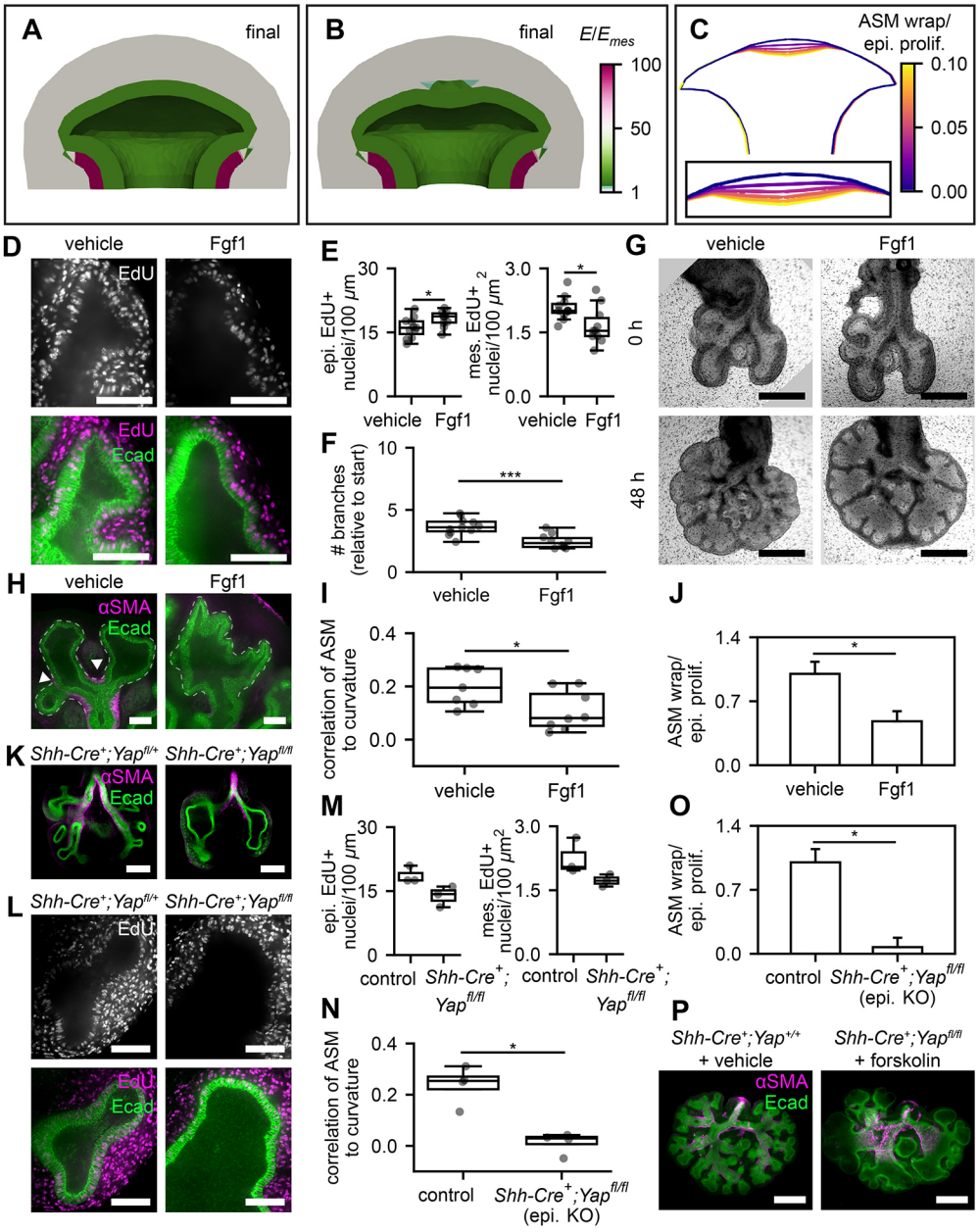

Fig. 7. Computational model predicts that branches are sculpted by the relative rates of ASM differentiation and epithelial proliferation. (A,B) Final geometry of simulations with no ASM at the tip of the epithelium (A) or the rate of ASM differentiation at the tip of the epithelium balanced with the rate of epithelial growth (ASM wrapping/epithelial proliferation=0.10) (B). (C) Final geometries of simulations with different relative rates of ASM differentiation and epithelial proliferation. Inset: magnified view of the cleft site. (D-J) Immunofluorescence analysis for Ecad and EdU (D), quantification of the density of EdU$^+$ epithelial (epi.) and mesenchymal (mes.) cells (*P*-values by unpaired, two-tailed Student's *t*-test: epi, 0.0381; mes, 0.0178) (E), quantification of the number of branches (*P*=0.000384 by unpaired, two-tailed Student's *t*-test) (F), bright-field images (G), immunofluorescence analysis for αSMA and Ecad (H), quantification of the correlation of αSMA staining intensity to epithelial curvature (*P*=0.0322 by unpaired, two-tailed Student's *t*-test) (I), and ratio of ASM wrapping to epithelial proliferation (*P*=0.0103 by a permutation test) (J) in E11.5 lungs cultured in the presence of Fgf1 or vehicle control for 48 h. (K-O) Immunofluorescence analysis for αSMA and Ecad (K) and Ecad and EdU (L), quantification of density of EdU$^+$ epithelial and mesenchymal cells (M), correlation of αSMA staining intensity to epithelial curvature (*P*=0.00192 by unpaired, two-tailed Student's *t*-test) (N) and ratio of ASM wrapping around branches to epithelial proliferation (*P*=0.0479 by a permutation test) (O) in E12-13 *Shh-Cre;Yap$^{fl/fl}$* (epi. KO) lungs compared with littermate controls. Shown are data from two (M) or four (N,O) independent experiments. (P) Immunofluorescence analysis for αSMA and Ecad in E11.5 epi. KO or littermate control lungs cultured in the presence of forskolin or vehicle control for 48 h. Bar graphs represent mean+s.e.m. In box-and-whisker plots, the midline, box, and whiskers represent the median, upper and lower quartiles, and furthest points, respectively, with the whiskers excluding outliers defined as points further than 1.5× interquartile range outside of the box limits. Scale bars: 50 µm (D,H,L); 500 µm (G); 250 µm (K); 200 µm (P).

dilated and buckled morphology instead of a properly branched epithelium.

Branching morphogenesis of the mouse lung thus appears to require growth of the airway epithelium and patterned stiffening of the surrounding mesenchyme, which serves as an external constraint to direct the growing epithelium into the bifurcations necessary to form a tree, akin to the mechanism proposed for branch formation in the human lung (Danopoulos et al., 2018; Warburton, 2021). The computational and experimental analyses presented here and in previous work (Goodwin et al., 2019; Kim et al., 2015) reveal

Development (2022) 149, dev199726. doi:10.1242/dev.199726

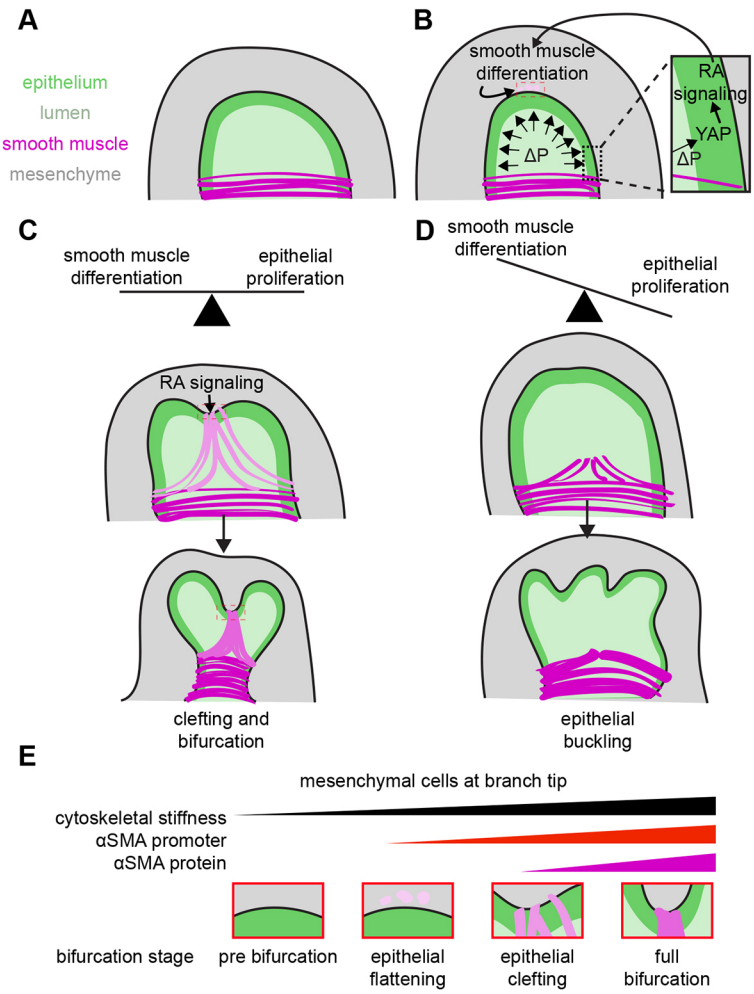

Fig. 8. Proposed mechanistic model. (A) Geometry of a lung branch before bifurcation. (B) High ΔP activates epithelial Yap, which promotes RA biosynthesis to control the rate of ASM differentiation relative to epithelial proliferation. (C) When the relative rates are balanced, the stiff ASM sculpts the epithelium into bifurcations. (D) When the epithelium proliferates faster than ASM differentiates, the tissue dilates and buckles. (E) Proposed physical, gene expression and cytoskeletal state of mesenchymal cells during epithelial bifurcation.

that this stiffening results from patterned differentiation of ASM. Curiously, a recent study reported that conditional knockout of the smooth muscle-associated transcription factor myocardin (*Myocd*) does not affect the ability of the lung to form branches (Young et al., 2020); based on this phenotype, the authors of that study concluded that the airway epithelium branches independently of ASM but did not propose an alternative mechanism for airway branching. What sculpts the branches in the *Myocd* knockout? It is possible that a non-cellular component of the mesenchyme, such as patterned deposition of ECM, provides sufficient constraint to direct airway epithelial branching in the absence of *Myocd*. However, our analysis here shows that the morphology of the epithelium is more closely correlated with the pattern of ASM than with that of fibronectin. Furthermore, when we replace the ASM layer in our computational model with a layer that has the thickness and stiffness of ECM, the epithelium fails to bifurcate (Fig. S7J-M), suggesting that matrix deposition is insufficient to act in this capacity.

It is also possible that the subepithelial mesenchymal cells in *Myocd*-knockout lungs retain their ability to sculpt epithelia by modifying their cytoskeletons and ECM interactions independently of *Myocd*. Although *Myocd* knockout decreases the expression of *Acta2* and *Myh11*, grouping genes by their functions and their biochemical pathways reveals that most genes involved in smooth muscle differentiation, cytoskeletal organization, contraction, and ECM adhesion are unaffected by loss of *Myocd* (Fig. S9). This observation is also consistent with our previous findings from fluorescent reporter mice, which revealed that the epithelium begins to bifurcate at the earliest stages of ASM differentiation, after the *Acta2* gene promoter has been activated but before αSMA protein can be detected in lungs imaged at low magnification (Kim et al., 2015). Finally, bioinformatics analysis of the ASM differentiation program reveals that nascent immature smooth muscle cells activate the expression of cytoskeletal components associated with cell stiffening before they begin expressing *Myocd* (Goodwin et al., 2020). Given the coupled dynamics of epithelial growth, ASM differentiation and branching morphogenesis, we postulate that the shape of the growing epithelium is influenced by this presumed gradual stiffening that occurs at the earliest stages of the ASM differentiation program; we predict that these stiffer, immature smooth muscle cells direct airway epithelial branching and that their presence is unaffected by knockout of *Myocd* (Fig. 8E). Therefore, patterned ASM differentiation directs the branching of the growing airway epithelium but *Myocd* expression does not.

It remains unclear how the spatial pattern of ASM is specified in the developing lung (Goodwin et al., 2019). In general, smooth muscle differentiation is controlled by both mechanical stretch (Jakkaraju et al., 2005) and soluble signals (Kim et al., 2015). Surprisingly, one study found that inhibiting RA led to modest increases in the expression of ASM markers (Chen et al., 2014). However, this previous work cultured explants in the presence of 10% serum, which can significantly alter the concentration of retinol (Engedal et al., 2006) and would also be expected to alter cell

Development (2022) 149, dev199726. doi:10.1242/dev.199726

proliferation, which can affect RA responsiveness in some tissues (Marcelo et al., 2013; Qiu et al., 2020). Here, we measured the distribution of αSMA protein, which forms the core of the smooth muscle cytoskeletal machinery (Jaslove and Nelson, 2018), and found that inhibiting RA decreases αSMA-positive cells at the tips of epithelial branches. Our observations support the conclusion that inhibiting RA decreases the rate of ASM differentiation.

Although the lung clearly develops in the presence of mechanical forces, our understanding of its mechanosensory and mechanotransduction machinery is still in its infancy. Our data reveal that ΔP promotes the nuclear translocation of Yap in the developing lung epithelium and activates the expression of genes with Tead-binding sites in their nearby regulatory regions. A central role for this mechanosensory pathway is supported by the phenotype of *Yap*-knockout animals, which fail to form lungs or initiate branching (Isago et al., 2020; Lin et al., 2017). It is likely that some of these defects are due to dysregulation of RA signaling. Consistent with our results, recent work has uncovered links between Yap nuclear localization and the expression of RA receptors and biosynthetic machinery in colorectal cancer cells (Bauzone et al., 2021).

Our findings identify RA signaling as one mechanism by which mechanical forces regulate morphogenesis in the developing lung. RA contributes to several developmental processes, from inner ear development to body-axis elongation (Cunningham and Duester, 2015; Ono et al., 2020), and is crucial for the formation of organs in which mechanical forces are also required for tissue growth, including the eye (Molotkov et al., 2006). However, few studies have investigated whether mechanical forces influence RA signaling or vice versa (Guo et al., 2016; Xiao et al., 2018). Our finding of a role for RA signaling in mechanotransduction downstream of Yap in the developing lung suggests that future studies might reveal a similar interplay between RA and Yap in the development of other tissues.

MATERIALS AND METHODS

Whole-lung RNA-seq bioinformatics analysis

Differential gene-expression analysis was carried out as previously described for an RNA-seq dataset of lungs cultured under high or low ΔP, available from the Gene Expression Omnibus with the GEO accession GSE90148 (Nelson et al., 2017). A custom Python script was created to identify sequences of DNase-hypersensitive regions near genes that were significantly differentially expressed under high versus low ΔP. Using the locations of DNase-hypersensitive regions from the mouse ENCODE lung DNase-hypersensitivity dataset (Yue et al., 2014), we generated a list of the locations of DNase-hypersensitive regions in the mm10 mouse genome build downloaded from the University of California, Santa Cruz (UCSC) genome browser (Kent et al., 2002). We then used the list of all NCBI Refseq mouse genes from the UCSC genome browser to locate the TSS of each gene. We compared the TSS of each gene to the start and end points of each DNase-hypersensitive region on the same chromosome and assigned each DNase-hypersensitive region as associated to the gene with the nearest TSS. We then extracted the sequences of all DNase-hypersensitive regions assigned to genes that were significantly increased under high ΔP as a FASTA file. This process was repeated on a list of random mouse genes generated by the Regulatory Sequence Analysis Tools web interface (Nguyen et al., 2018) to obtain a FASTA file of background sequences. The high ΔP FASTA file was assayed for motifs that were overrepresented relative to the background file using the HOMER findMotifs.pl FASTA motif analysis script (Heinz et al., 2010). Gene identifiers were converted between Refseq and official gene-symbol formats using DAVID (Huang et al., 2009a,b). To determine whether genes involved in RA signaling depend on the expression of Yap in the airway epithelium, we analyzed a previously published bulk RNA-seq dataset (GSE93339) from E12.5 lungs of *Shh-Cre*$^{+}$*;Yap*$^{fl/fl}$ embryos and littermate controls (Lin et al., 2017). For each gene of interest, we retrieved the $\log_2$ fold changes and adjusted *P*-values provided in this GEO entry. We also obtained published bulk RNA-seq data from E13.5 lungs (five controls and five mutants) in which *Myocd* had been deleted from the mesenchyme (GSE143394; Young et al., 2020). Data were processed using the DESeq2 package (Love et al., 2014), which was used to import data and estimate size factors and dispersions. DESeq2 was then used to calculate differential expression of genes and their significance using the Wald test. We focused on genes from GO biological process terms and KEGG signaling pathway terms involved in cell contractility and adhesion. We then used volcano plots to visualize adjusted *P*-values and $\log_2$ fold changes for each of these gene sets.

scRNA-seq analysis

Left lobes from E11.5 mouse lungs were treated with dispase for 10 min, dissociated with tungsten needles, and resuspended in DMEM without HEPES supplemented with 5% fetal bovine serum (FBS). The resulting solution was passed through a 40-µm-diameter pore filter. Samples were then processed at the Princeton Genomics Core Facility on a 10x Genomics Chromium Controller and with an Illumina Nextera library prep kit to barcode and reverse-transcribe RNA from single cells, and the cDNA was sequenced using an Illumina HiSeq 2500 Rapid Flow Cell to generate paired-end reads. FASTQ base calling was performed using 10x CellRanger software. The resulting sequence files were processed using the R Bioconductor package Seurat 3.0 to scale the data, find variable features and perform cell-stage correction and cell clustering based on expression of known markers of cell types in the developing lung (Butler et al., 2018; Stuart et al., 2019). Blood cells were removed at this stage to focus the analysis on native lung cell types. scRNA-seq data are available from the Gene Expression Omnibus with the GEO accession GSE153069 (Goodwin et al., 2020). Transcriptional differences between proximal and distal epithelial cell identities were investigated using a previously published dataset (GSE144170) of scRNA-seq data from airway epithelial cells isolated at E15.5 (Gerner-Mauro et al., 2020) also processed with Seurat. Only cells expressing *Cdh1* were included. To focus on proximal and distal cell types, cells were classified based on whether they expressed *Sox2*, *Sox9* or neither.

Mouse husbandry

CD1 mice were obtained from Charles River. *RARE-hsp68lacZ* RA receptor activation reporter (*RARE-lacZ*; JAX 008477) (Rossant et al., 1991), *Shh-Cre-EGFP* (*Shh-Cre*; JAX 005622) and *Yap-flox/flox* (*Yap*$^{fl/fl}$; JAX 027929) mice were obtained from the Jackson Laboratory. Breeding pairs were set up locally for timed pregnancy. *Yap*$^{fl/fl}$*;RARE-lacZ* females were generated by breeding *Yap*$^{fl/fl}$ mice with *RARE-lacZ* mice and *Shh-Cre*$^{+}$*;Yap*$^{fl/+}$ males were generated by breeding *Yap*$^{fl/fl}$ mice with *Shh-Cre*$^{+}$ mice. *Yap*$^{fl/fl}$*;RARE-lacZ* females were mated with *Shh-Cre*$^{+}$*;Yap*$^{fl/+}$ males to generate timed pregnancies of *Shh-Cre*;*Yap*$^{fl/fl}$*;RARE-lacZ* (lung epithelial Yap knockout) and littermate control RARE reporter embryos. Pups and embryos were genotyped by PCR and gel electrophoresis on DNA extracted from pup tail-snips or embryo hindlimbs and tails. All primers used for genotyping are listed in Table S2. Embryos were isolated in accordance with institutional guidelines following the National Institutes of Health Guide for the Care and Use of Laboratory Animals and approved by the Princeton University Institutional Animal Care and Use Committee.

Embryonic lung explant culture

Lungs were dissected and cultured as explants as previously described (Kim et al., 2015). Briefly, lungs were dissected from embryos in cold phosphate buffered saline (PBS) supplemented with 1% penicillin/streptomycin (Gibco, Thermo Fisher Scientific). Explants were cultured on microetched nucleopore filters (8 µm pore size, 25 mm diameter; Whatman) in DMEM/F12 medium without HEPES buffer (HyClone, GE) supplemented with 5% filtered, heat-inactivated FBS and 1% penicillin/streptomycin (Gibco). Explants were treated with BMS493 (1 µM, Sigma-Aldrich), nitrofen (5 µM, Sigma-Aldrich), forskolin (5 µM, Sigma-Aldrich), verteporfin (2 µM, Sigma-Aldrich), or dimethyl sulfoxide (DMSO) vehicle control

Development (2022) 149, dev199726. doi:10.1242/dev.199726

(ATCC), or Fgf1 (1 µg, R&D Systems) or PBS vehicle control. Medium was replaced every 24 h in all explant culture experiments. Cell proliferation was measured by EdU incorporation using a Click-iT EdU Imaging Kit (Invitrogen) by incubating lungs at 37°C with 20 µM EdU for 30 min. In culture experiments, EdU was added directly to the culture medium; in *Yap* epithelial knockout experiments, lungs were dissected and cultured on nucleopore filters for 1 h before adding EdU to the culture medium.

Cell culture

Primary mesenchymal cells were harvested from E11.5 CD1 or *RARE-lacZ* mouse lungs using a differential plating technique (Schuger et al., 1993). Briefly, lungs were digested with 0.25% trypsin and 0.05% EDTA (Gibco) while pipetting vigorously. Homogenized mixtures of embryonic lung cells were allowed to attach directly onto microcontact-printed islands of fibronectin for 1 h before unattached cells were washed off with PBS and new medium was added, allowing only enough time for mesenchymal cells to attach. Cells were cultured in Eagle's Minimal Essential Medium (EMEM; ATCC) supplemented with 10% FBS, 1% penicillin/streptomycin, and 50 µg/ml gentamycin (Gibco). Cultures were treated with BMS493 (1 µM) or DMSO vehicle control where indicated.

Microcontact printing

Regularly spaced 30-µm-wide squares or lines of fibronectin were microcontact printed onto UVO-treated polydimethylsiloxane (PDMS)-coated glass coverslips using sterile stamps of PDMS that were adsorbed with fibronectin (25 µg/ml, Corning) in PBS at 4°C overnight and dried under compressed nitrogen (Gomez and Nelson, 2011). Coverslips were then passivated using a solution of 1% synperonic F108 (Fluka) for 20 min and washed twice with PBS.

Quantitative real time-PCR (qRT-PCR) analysis

Total RNA was extracted using TRIzol® reagent according to the manufacturer's instructions, followed by cDNA synthesis using the Verso cDNA synthesis kit with poly(dT) primers (Thermo Fisher Scientific). Transcript levels were measured by qRT-PCR using an Applied Biosystems StepOne Plus instrument and iTaq Universal SYBR Green Supermix (Bio-Rad). Amplification was followed by melting-curve analysis to verify the presence of a single PCR product. Primers specific for each target are listed in Table S3. The relative expression of each transcript was quantified using the $\Delta\Delta C_T$ method with the 18S ribosomal subunit as the calibrator in each sample (Schmittgen and Livak, 2008). The efficiency of each primer was between 90 and 105% (Schmittgen and Livak, 2008) according to a standard curve of serially diluted template.

Immunofluorescence analysis

Cells were fixed with 4% paraformaldehyde (PFA; Fisher) for 15 min, permeabilized in 0.5% Triton X-100 (PBS-T), blocked in PBS-T supplemented with 10% FBS, incubated with primary antibody for 1 h at room temperature, washed, blocked, incubated with secondary antibody for 1 h at room temperature, and mounted with Fluoromount-G (Southern Biotech). Lungs were fixed, permeabilized in 0.1% PBS-T, blocked in PBS-T supplemented with 5% FBS and 0.1% bovine serum albumin (BSA; Sigma-Aldrich), incubated overnight with primary antibody at 4°C, washed, and incubated overnight with secondary antibody at 4°C. Cells and lungs were counterstained with Hoechst 33342 (Invitrogen). The antibody sources, targets and dilutions are listed in Table S4. Lungs were dehydrated progressively in methanol and cleared in 1:2 benzyl alcohol: benzyl benzoate (Murray's clear).

Imaging and image analysis

Immunostained samples were imaged on a Nikon Ti-U inverted microscope with a Hamamatsu camera and a spinning disk confocal attachment (X-Light) using a Plan Apo 4× 0.2 NA, S Plan Fluor 20× 0.45 NA or Plan Fluor 40× oil 1.3 NA objective. Tiled images were stitched together using the stitching plugin (Preibisch et al., 2009) for the ImageJ FIJI distribution (Schneider et al., 2012). Branching morphogenesis was quantified by counting the number of terminal branches in confocal stacks using the FIJI cell counter plugin. Brightfield stacks taken on a Leica M205FA stereomicroscope were processed with the FIJI linear stack alignment with SIFT and extended depth-of-field plugins (Forster et al., 2004). Displayed images of sections were white-balanced in FIJI. X-gal staining intensity was quantified with a custom MATLAB script by outlining the whole lung, epithelium or mesenchyme, adding together the average red, green and blue (RGB) values of the selected area and subtracting the sum of the RGB values of a random background area from the bright-field images. Smooth muscle wrapping around epithelial branches was measured by finding the Pearson correlation between epithelial curvature (concave versus convex regions) and αSMA staining intensity along the outline of each epithelial branch. αSMA staining intensity was determined by outlining the epithelium in a confocal slice through the widest portion of a branch and taking a maximum projection of the αSMA staining at each point along the outline. The magnitude of curvature $\left(\kappa = \frac{1}{radius}\right)$ was calculated by constructing a triangle using the points on the path 5 pixels before and after each point and finding the radius of the circle circumscribed around the triangle. After skeletonizing the lung based on the epithelial outline, a positive curvature was assigned if the vector between the skeleton and the point was in the same direction as the vector between the point and center of curvature, and negative otherwise. EdU incorporation was quantified by selecting a confocal slice through the airway epithelium, counting the number of EdU^+ nuclei per length of epithelium, and averaging over one to three separate branches on each lung using a custom MATLAB script. Intensity of αSMA staining in micropatterned cells was measured by sum-projecting confocal stacks and quantifying cell shape and the total intensity of staining using a custom MATLAB script. Yap1 quantifications were also performed using a custom MATLAB script. First, images were background-subtracted, then nuclear masks were generated based on Hoechst staining. Yap1 pixel intensities within or outside of nuclei in the airway epithelium were then measured in five randomly selected regions of interest per confocal stack. We then took the ratio of nuclear to cytoplasmic intensity as a readout of Yap activity.

X-gal staining

LacZ-expressing tissues were stained with X-gal by fixing for 30 min in 1% formaldehyde, 0.2% glutaraldehyde, 2 mM $MgCl_2$, 5 mM EGTA, 0.02% tergitol (NP-40), permeabilizing with 0.02% tergitol, staining at 4°C or room temperature from 4 h to overnight in a solution of 5 mM $K_3Fe(CN)_6$, 2 mM $MgCl_2$, 0.01% sodium deoxycholate, 0.02% tergitol and 1 mg/ml X-gal, and post-fixing with 4% PFA. Stained tissues were either cleared in 75% glycerol and imaged in wholemount on a Leica M205FA stereomicroscope or embedded in optimal cutting temperature compound (OCT), cut into 10-µm-thick sections on a Leica CM3050S cryostat, mounted with Fluoromount-G and imaged on a Nikon Eclipse TS100 with an attached Nikon CoolPix camera or Leica M205FA stereomicroscope. To examine X-gal stain in epithelial rudiments denuded of mesenchyme, lungs from *RARE-lacZ* reporter mice were explanted and incubated at room temperature for 5 min in dispase (Corning), which was subsequently inactivated in DMEM:F12 media supplemented with 5% FBS and 0.1% BSA. Tungsten needles (Fine Science Tools) were then used to remove the mesenchyme and the resulting epithelial rudiments were fixed and stained with X-gal as described above.

In situ hybridization

Probe sequences were generated by PCR (primers listed in Table S5) from embryonic mouse lung cDNA and ligated into a dual promoter pCRII-TOPO vector (Invitrogen) that was transformed into Max Efficiency DH5α chemically competent cells (Invitrogen) for amplification. Plasmids were harvested using a Qiagen Midi Prep kit and digested using the appropriate restriction enzymes for each promoter. Antisense and sense digoxigenin-uridine-5′-triphosphate (UTP)-labeled riboprobes were synthesized using a DIG RNA Labeling Kit (SP6/T7) (Roche) and purified using quick spin columns for radiolabeled RNA purification (Roche). Explanted lungs were fixed in 4% paraformaldehyde overnight, dehydrated in methanol, rehydrated and digested with Proteinase K (Ambion) before incubating with probe overnight at hybridization temperature in a Bambino

Development (2022) 149, dev199726. doi:10.1242/dev.199726

Hybridization Oven (Boekel Scientific). Hybridized tissues were probed with AP-anti-DIG antibody Fab fragment (Roche) and color was developed using nitro blue tetrazolium chloride (NBT; Roche) and 5-bromo-4-chloro-3-indolyl-phosphate (BCIP; Roche) solutions. Stained tissues were cleared in 75% glycerol and imaged in wholemount on a Leica M205FA stereomicroscope.

Computational modeling

An idealized 3D model and finite-element mesh of an epithelial branch surrounded by smooth muscle and undifferentiated mesenchyme were created using the computer-aided design functionality of Gmsh (Geuzaine and Remacle, 2009). As described previously (Goodwin et al., 2019), the epithelium, mesenchyme, and smooth muscle compartments were modeled as connected hyperelastic solids, each with different elastic moduli. Epithelial growth was modeled as an isotropic expansion of the size of the epithelial layer in a plane tangential to the epithelium at each point. The FEniCS Python module (Logg et al., 2012) was used to numerically minimize the potential energy at each timestep as the epithelium grew. The results were visualized and plotted using ParaView (Squillacote and Ahrens, 2006) and the Matplotlib Python package. Additional details on the mathematical formulation of the problem are available in supplementary Materials and Methods.

Statistical analysis

Statistical analyses were carried out using the Python SciPy Stats and statsmodels packages or Microsoft Excel. Unpaired, two-tailed Student's *t*-tests were used for pairwise comparisons and ANOVA with Tukey's post-hoc test was used to compare more than two groups. Statistical significance in figures is denoted as $*P<0.05$, $**P<0.01$ and $***P<0.001$ and exact values for significant results are noted in the figure legends. In box-and-whisker plots, the midline, box, and whiskers represent the median, upper and lower quartiles, and furthest points, respectively, with the whiskers excluding outliers defined as points further than 1.5× interquartile range outside of the box limits. Individual data points on graphs represent individual lungs from three independent experiments, except where noted. The standard error of the mean (s.e.m.) of ASM wrapping to epithelial proliferation ratios was calculated by error propagation of the s.e.m. from the correlation of ASM to curvature and epithelial proliferation. Permutation tests to compare ASM wrapping to epithelial proliferation were carried out by defining a test statistic $T = \frac{muscle\,wrapping_{control}}{proliferation_{control}} - \frac{muscle\,wrapping_{treatment}}{proliferation_{treatment}}$, then randomly reassigning the ASM wrapping and proliferation data points to treatment or control groups and calculating the test statistic 10,000 times. The *P*-value was calculated by finding the proportion of permuted T that had a larger absolute value than the experimentally determined T.

Acknowledgements

We are grateful to Sarah Paramore and other members of the Tissue Morphodynamics Group for helpful discussions and experimental assistance, and Lance Parsons of the Princeton Genomics Core for assistance in processing bulk RNA-seq data.

Competing interests

The authors declare no competing or financial interests.

Author contributions

Conceptualization: J.M.J., C.M.N.; Software: J.M.J., S.M.; Formal analysis: J.M.J., K.G., S.M.; Investigation: J.M.J., K.G., A.S., J.W.S.; Writing - original draft: J.M.J.; Writing - review & editing: A.K., C.M.N.; Supervision: A.K., C.M.N.; Project administration: C.M.N.; Funding acquisition: C.M.N.

Funding

This work was supported in part by grants (HL110335, HL118532, HL120142 and HD0990300) and National Research Service Award (NRSA) Fellowships (HL139039 to J.M.J. and HL137273 to J.W.S.) from the National Institutes of Health. K.G. was supported in part by a postgraduate scholarship-doctoral (PGS-D) from the Natural Sciences and Engineering Research Council of Canada and the Dr Margaret McWilliams Predoctoral Fellowship from the Canadian Federation of University Women. C.M.N. was supported in part by a Faculty Scholars Award from the Howard Hughes Medical Institute. Deposited in PMC for release after 12 months.

Data availability

scRNA-seq data are available from the Gene Expression Omnibus under accession number GSE153069.

References

Al Tanoury, Z., Piskunov, A., Andriamoratsiresy, D., Gaouar, S., Lutzing, R., Ye, T., Jost, B., Keime, C. and Rochette-Egly, C. (2014). Genes involved in cell adhesion and signaling: a new repertoire of retinoic acid receptor target genes in mouse embryonic fibroblasts. *J. Cell Sci.* **127**, 521-533. doi:10.1242/jcs.131946

Alcaraz, J., Buscemi, L., Grabulosa, M., Trepat, X., Fabry, B., Farré, R. and Navajas, D. (2003). Microrheology of human lung epithelial cells measured by atomic force microscopy. *Biophys. J.* **84**, 2071-2079. doi:10.1016/S0006-3495(03)75014-0

Bauzone, M., Souidi, M., Dessein, A.-F., Wisztorski, M., Vincent, A., Gimeno, J.-P., Monte, D., Van Seuningen, I., Gespach, C. and Huet, G. (2021). Cross-talk between YAP and RAR-RXR drives expression of stemness genes to promote 5-FU resistance and self-renewal in colorectal cancer cells. *Mol. Cancer Res.* **19**, 612-622. doi:10.1158/1541-7786.MCR-20-0462

Belik, J., Davidge, S. T., Zhang, W., Pan, J. and Greer, J. J. (2003). Airway smooth muscle changes in the nitrofen-induced congenital diaphragmatic hernia rat model. *Pediatr. Res.* **53**, 737-743. doi:10.1203/01.PDR.0000057986.74037.7B

Beurskens, N., Klaassens, M., Rottier, R., de Klein, A. and Tibboel, D. (2007). Linking animal models to human congenital diaphragmatic hernia. *Birth Defects Res. A Clin. Mol. Teratol.* **79**, 565-572. doi:10.1002/bdra.20370

Butler, A., Hoffman, P., Smibert, P., Papalexi, E. and Satija, R. (2018). Integrating single-cell transcriptomic data across different conditions, technologies, and species. *Nat. Biotechnol.* **36**, 411-420. doi:10.1038/nbt.4096

Cardoso, W. V., Williams, M. C., Mitsialis, S. A., Joyce-Brady, M., Rishi, A. K. and Brody, J. S. (1995). Retinoic acid induces changes in the pattern of airway branching and alters epithelial cell differentiation in the developing lung in vitro. *Am. J. Respir. Cell Mol. Biol.* **12**, 464-476. doi:10.1165/ajrcmb.12.5.7742011

Chandrasekharan, P. K., Rawat, M., Madappa, R., Rothstein, D. H. and Lakshminrusimha, S. (2017). Congenital Diaphragmatic hernia - a review. *Matern. Health Neonatol. Perinatol.* **3**, 6. doi:10.1186/s40748-017-0045-1

Chazaud, C., Dollé, P., Rossant, J. and Mollard, R. (2003). Retinoic acid signaling regulates murine bronchial tubule formation. *Mech. Dev.* **120**, 691-700. doi:10.1016/S0925-4773(03)00048-0

Chen, C. Y. and Schwartz, R. J. (1997). Competition between negative acting YY1 versus positive acting serum response factor and tinman homologue Nkx-2.5 regulates cardiac alpha-actin promoter activity. *Mol. Endocrinol.* **11**, 812-822. doi:10.1210/me.11.6.812

Chen, F., Desai, T. J., Qian, J., Niederreither, K., Lü, J. and Cardoso, W. V. (2007). Inhibition of Tgf beta signaling by endogenous retinoic acid is essential for primary lung bud induction. *Development* **134**, 2969-2979. doi:10.1242/dev.006221

Chen, F., Cao, Y., Qian, J., Shao, F., Niederreither, K. and Cardoso, W. V. (2010). A retinoic acid-dependent network in the foregut controls formation of the mouse lung primordium. *J. Clin. Invest.* **120**, 2040-2048. doi:10.1172/JCI40253

Chen, F., Marquez, H., Kim, Y. K., Qian, J., Shao, F., Fine, A., Cruikshank, W. W., Quadro, L. and Cardoso, W. V. (2014). Prenatal retinoid deficiency leads to airway hyperresponsiveness in adult mice. *J. Clin. Invest.* **124**, 801-811. doi:10.1172/JCI70291

Chen, F., Shao, F., Hinds, A., Yao, S., Ram-Mohan, S., Norman, T. A., Krishnan, R. and Fine, A. (2018). Retinoic acid signaling is essential for airway smooth muscle homeostasis. *JCI Insight* **3**, 1-17. doi:10.1172/jci.insight.120398

Cheng, Y., Ma, Z., Kim, B.-H., Wu, W., Cayting, P., Boyle, A. P., Sundaram, V., Xing, X., Dogan, N., Li, J. et al. (2014). Principles of regulatory information conservation between mouse and human. *Nature* **515**, 371-375. doi:10.1038/nature13985

Chevalier, N. R., Gazguez, E., Dufour, S. and Fleury, V. (2016). Measuring the micromechanical properties of embryonic tissues. *Methods* **94**, 120-128. doi:10.1016/j.ymeth.2015.08.001

Chinoy, M. R., Chi, X. and Cilley, R. E. (2001). Down-regulation of regulatory proteins for differentiation and proliferation in murine fetal hypoplastic lungs: altered mesenchymal-epithelial interactions. *Pediatr. Pulmonol.* **32**, 129-141. doi:10.1002/ppul.1099

Clugston, R. D., Zhang, W., Álvarez, S., de Lera, A. R. and Greer, J. J. (2010). Understanding abnormal retinoid signaling as a causative mechanism in congenital diaphragmatic hernia. *Am. J. Respir. Cell Mol. Biol.* **42**, 276-285. doi:10.1165/rcmb.2009-0076OC

Cunningham, T. J. and Duester, G. (2015). Mechanisms of retinoic acid signalling and its roles in organ and limb development. *Nat. Rev. Mol. Cell Biol.* **16**, 110-123. doi:10.1038/nrm3932

Danopoulos, S., Alonso, I., Thornton, M. E., Grubbs, B. H., Bellusci, S., Warburton, D. and Al Alam, D. (2018). Human lung branching morphogenesis is orchestrated by the spatiotemporal distribution of ACTA2, SOX2, and SOX9. *Am. J. Physiol. Lung Cell. Mol. Physiol.* **314**, L144-L149. doi:10.1152/ajplung.00379.2017

Dekkers, J. F., Wiegerinck, C. L., de Jonge, H. R., Bronsveld, I., Janssens, H. M., de Winter-de Groot, K. M., Brandsma, A. M., de Jong, N. W. M., Bijvelds, M. J. C., Scholte, B. J. et al. (2013). A functional CFTR assay using primary cystic fibrosis intestinal organoids. *Nat. Med.* **19**, 939-945. doi:10.1038/nm.3201

Encode Project Consortium, Moore, J. E., Purcaro, M. J., Pratt, H. E., Epstein, C. B., Shoresh, N., Adrian, J., Kawli, T., Davis, C. A., Dobin, A. et al. (2020). Expanded encyclopaedias of DNA elements in the human and mouse genomes. *Nature* **583**, 699-710. doi:10.1038/s41586-020-2493-4

Engedal, N., Gjevik, T., Blomhoff, R. and Blomhoff, H. K. (2006). All-trans retinoic acid stimulates IL-2-mediated proliferation of human T lymphocytes: early induction of cyclin D3. *J. Immunol.* **177**, 2851-2861. doi:10.4049/jimmunol.177.5.2851

Fernandes-Silva, H., Araújo-Silva, H., Correia-Pinto, J. and Moura, R. S. (2020). Retinoic acid: a key regulator of lung development. *Biomolecules* **10**, 1-18. doi:10.3390/biom10010152

Forster, B., Van De Ville, D., Berent, J., Sage, D. and Unser, M. (2004). Complex wavelets for extended depth-of-field: a new method for the fusion of multichannel microscopy images. *Microsc. Res. Tech.* **65**, 33-42. doi:10.1002/jemt.20092

Fujii, S., Muranaka, T., Matsubayashi, J., Yamada, S., Yoneyama, A. and Takakuwa, T. (2020). The bronchial tree of the human embryo: an analysis of variations in the bronchial segments. *J. Anat.* **237**, 311-322. doi:10.1111/joa.13199

George, U. Z., Bokka, K. K., Warburton, D. and Lubkin, S. R. (2015). Quantifying stretch and secretion in the embryonic lung: implications for morphogenesis. *Mech. Dev.* **138**, 356-363. doi:10.1016/j.mod.2015.07.003

Gerner-Mauro, K. N., Akiyama, H. and Chen, J. (2020). Redundant and additive functions of the four Lef/Tcf transcription factors in lung epithelial progenitors. *Proc. Natl. Acad. Sci. USA* **117**, 12182-12191. doi:10.1073/pnas.2002082117

Geuzaine, C. and Remacle, J.-F. (2009). Gmsh: A 3-D finite element mesh generator with built-in pre- and post-processing facilities. *Int. J. Numer. Meth. Eng.* **79**, 1309-1331. doi:10.1002/nme.2579

Gomez, E. W. and Nelson, C. M. (2011). Lithographically defined two- and three-dimensional tissue microarrays. *Methods Mol. Biol.* **671**, 107-116. doi:10.1007/978-1-59745-551-0_5

Goodwin, K., Mao, S., Guyomar, T., Miller, E., Radisky, D. C., Košmrlj, A. and Nelson, C. M. (2019). Smooth muscle differentiation shapes domain branches during mouse lung development. *Development* **146**, dev181172. doi:10.1242/dev.181172

Goodwin, K., Jaslove, J. M., Tao, H., Zhu, M., Hopyan, S. and Nelson, C. M. (2020). Patterning the embryonic pulmonary mesenchyme. *iScience* (in press).

Guo, P.-D., Lu, X.-X., Gan, W.-J., Li, X.-M., He, X.-S., Zhang, S., Ji, Q.-H., Zhou, F., Cao, Y., Wang, J.-R. et al. (2016). RARgamma downregulation contributes to colorectal tumorigenesis and metastasis by derepressing the Hippo-Yap pathway. *Cancer Res.* **76**, 3813-3825. doi:10.1158/0008-5472.CAN-15-2882

Han, S., Pang, M.-F. and Nelson, C. M. (2018). Substratum stiffness tunes proliferation downstream of Wnt3a in part by regulating integrin-linked kinase and frizzled-1. *J. Cell Sci.* **131**, jcs210476. doi:10.1242/jcs.210476

Harding, R. and Hooper, S. B. (1996). Regulation of lung expansion and lung growth before birth. *J. Appl. Physiol. (1985)* **81**, 209-224. doi:10.1152/jappl.1996.81.1.209

He, P., Williams, B. A., Trout, D., Marinov, G. K., Amrhein, H., Berghella, L., Goh, S.-T., Plajzer-Frick, I., Afzal, V., Pennacchio, L. A. et al. (2020). The changing mouse embryo transcriptome at whole tissue and single-cell resolution. *Nature* **583**, 760-767. doi:10.1038/s41586-020-2536-x

Heinz, S., Benner, C., Spann, N., Bertolino, E., Lin, Y. C., Laslo, P., Cheng, J. X., Murre, C., Singh, H. and Glass, C. K. (2010). Simple combinations of lineage-determining transcription factors prime cis-regulatory elements required for macrophage and B cell identities. *Mol. Cell* **38**, 576-589. doi:10.1016/j.molcel.2010.05.004

Herriges, M. and Morrisey, E. E. (2014). Lung development: orchestrating the generation and regeneration of a complex organ. *Development* **141**, 502-513. doi:10.1242/dev.098186

Hu, B., Wu, Y. M., Wu, Z. and Phan, S. H. (2010). Nkx2.5/Csx represses myofibroblast differentiation. *Am. J. Respir. Cell Mol. Biol.* **42**, 218-226. doi:10.1165/rcmb.2008-0404OC

Huang, D. W., Sherman, B. T. and Lempicki, R. A. (2009a). Bioinformatics enrichment tools: paths toward the comprehensive functional analysis of large gene lists. *Nucleic Acids Res.* **37**, 1-13. doi:10.1093/nar/gkn923

Huang, D. W., Sherman, B. T. and Lempicki, R. A. (2009b). Systematic and integrative analysis of large gene lists using DAVID bioinformatics resources. *Nat. Protoc.* **4**, 44-57. doi:10.1038/nprot.2008.211

Huraskin, D., Eiber, N., Reichel, M., Zidek, L. M., Kravic, B., Bernkopf, D., von Maltzahn, J., Behrens, J. and Hashemolhosseini, S. (2016). Wnt/β-catenin signaling via Axin2 is required for myogenesis and, together with YAP/Taz and Tead1, active in IIa/IIx muscle fibers. *Development* **143**, 3128-3142. doi:10.1242/dev.139907

Isago, H., Mitani, A., Mikami, Y., Horie, M., Urushiyama, H., Hamamoto, R., Terasaki, Y. and Nagase, T. (2020). Epithelial expression of YAP and TAZ is sequentially required in lung development. *Am. J. Respir. Cell Mol. Biol.* **62**, 256-266. doi:10.1165/rcmb.2019-0218OC

Jakkaraju, S., Zhe, X., Pan, D., Choudhury, R. and Schuger, L. (2005). TIPs are tension-responsive proteins involved in myogenic versus adipogenic differentiation. *Dev. Cell* **9**, 39-49. doi:10.1016/j.devcel.2005.04.015

Jaslove, J. M. and Nelson, C. M. (2018). Smooth muscle: a stiff sculptor of epithelial shapes. *Philos. Trans. R. Soc. Lond. B Biol. Sci.* **373**, 1-12. doi:10.1098/rstb.2017.0318

Keijzer, R., Liu, J., Deimling, J., Tibboel, D. and Post, M. (2000). Dual-hit hypothesis explains pulmonary hypoplasia in the nitrofen model of congenital diaphragmatic hernia. *Am. J. Pathol.* **156**, 1299-1306. doi:10.1016/S0002-9440(10)65000-6

Kent, W. J., Sugnet, C. W., Furey, T. S., Roskin, K. M., Pringle, T. H., Zahler, A. M. and Haussler, D. (2002). The human genome browser at UCSC. *Genome Res.* **12**, 996-1006. doi:10.1101/gr.229102

Kim, H. Y., Pang, M.-F., Varner, V. D., Kojima, L., Miller, E., Radisky, D. C. and Nelson, C. M. (2015). Localized smooth muscle differentiation Is essential for epithelial bifurcation during branching morphogenesis of the mammalian lung. *Dev. Cell* **34**, 719-726. doi:10.1016/j.devcel.2015.08.012

Li, L., Miano, J. M., Cserjesi, P. and Olson, E. N. (1996). SM22α, a marker of adult smooth muscle, is expressed in multiple myogenic lineages during embryogenesis. *Circ. Res.* **78**, 188-195. doi:10.1161/01.RES.78.2.188

Lin, C., Yao, E., Zhang, K., Jiang, X., Croll, S., Thompson-Peer, K. and Chuang, P.-T. (2017). YAP is essential for mechanical force production and epithelial cell proliferation during lung branching morphogenesis. *eLife* **6**, e21130. doi:10.7554/eLife.21130

Liu, R., Hossain, M. M., Chen, X. and Jin, J.-P. (2017). Mechanoregulation of SM22α/Transgelin. *Biochemistry* **56**, 5526-5538. doi:10.1021/acs.biochem.7b00794

Liu-Chittenden, Y., Huang, B., Shim, J. S., Chen, Q., Lee, S.-J., Anders, R. A., Liu, J. O. and Pan, D. (2012). Genetic and pharmacological disruption of the TEAD-YAP complex suppresses the oncogenic activity of YAP. *Genes Dev.* **26**, 1300-1305. doi:10.1101/gad.192856.112

Logg, A., Mardal, K.-A. and Wells, G. (2012). *Automated Solution of Differential Equations by the Finite Element Method: The FEniCS Book*. Heidelberg: Springer.

Loo, C. K. C., Pearen, M. A., Pereira, T. N., Perry-Keene, J., Payton, D. and Ramm, G. A. (2018). Lung and liver growth and retinoic acid status in human fetuses with congenital diaphragmatic hernia. *Early Hum. Dev.* **116**, 17-23. doi:10.1016/j.earlhumdev.2017.10.005

Love, M. I., Huber, W. and Anders, S. (2014). Moderated estimation of fold change and dispersion for RNA-seq data with DESeq2. *Genome Biol.* **15**, 550. doi:10.1186/s13059-014-0550-8

Major, D., Cadenas, M., Fournier, L., Leclerc, S., Lefebvre, M. and Cloutier, R. (1998). Retinol status of newborn infants with congenital diaphragmatic hernia. *Pediatr. Surg. Int.* **13**, 547-549. doi:10.1007/s003830050399

Malpel, S., Mendelsohn, C. and Cardoso, W. V. (2000). Regulation of retinoic acid signaling during lung morphogenesis. *Development* **127**, 3057-3067. doi:10.1242/dev.127.14.3057

Marcelo, K. L., Sills, T. M., Coskun, S., Vasavada, H., Sanglikar, S., Goldie, L. C. and Hirschi, K. K. (2013). Hemogenic endothelial cell specification requires c-Kit, Notch signaling, and p27-mediated cell-cycle control. *Dev. Cell* **27**, 504-515. doi:10.1016/j.devcel.2013.11.004

Mayor, R., Morgan, R. and Sargent, M. G. (1995). Induction of the prospective neural crest of Xenopus. *Development* **121**, 767-777. doi:10.1242/dev.121.3.767

Metzger, R. J., Klein, O. D., Martin, G. R. and Krasnow, M. A. (2008). The branching programme of mouse lung development. *Nature* **453**, 745-750. doi:10.1038/nature07005

Mey, J., Babiuk, R. P., Clugston, R., Zhang, W. and Greer, J. J. (2003). Retinal dehydrogenase-2 is inhibited by compounds that induce congenital diaphragmatic hernias in rodents. *Am. J. Pathol.* **162**, 673-679. doi:10.1016/S0002-9440(10)63861-8

Mezquita, B., Mezquita, P., Pau, M., Gasa, L., Navarro, L., Samitier, M., Pons, M. and Mezquita, C. (2018). All-trans-retinoic acid activates the pro-invasive Src-YAP-Interleukin 6 axis in triple-negative MDA-MB-231 breast cancer cells while cerivastatin reverses this action. *Sci. Rep.* **8**, 7047. doi:10.1038/s41598-018-25526-1

Mollard, R., Ghyselinck, N. B., Wendling, O., Chambon, P. and Mark, M. (2000). Stage-dependent responses of the developing lung to retinoic acid signaling. *Int. J. Dev. Biol.* **44**, 457-462.

Molotkov, A., Molotkova, N. and Duester, G. (2006). Retinoic acid guides eye morphogenetic movements via paracrine signaling but is unnecessary for retinal dorsoventral patterning. *Development* **133**, 1901-1910. doi:10.1242/dev.02328

Montedonico, S., Nakazawa, N. and Puri, P. (2006). Retinoic acid rescues lung hypoplasia in nitrofen-induced hypoplastic foetal rat lung explants. *Pediatr. Surg. Int.* **22**, 2-8. doi:10.1007/s00383-005-1571-x

Montedonico, S., Nakazawa, N. and Puri, P. (2008a). Congenital diaphragmatic hernia and retinoids: searching for an etiology. *Pediatr. Surg. Int.* **24**, 755-761. doi:10.1007/s00383-008-2140-x

Montedonico, S., Sugimoto, K., Felle, P., Bannigan, J. and Puri, P. (2008b). Prenatal treatment with retinoic acid promotes pulmonary alveologenesis in the nitrofen model of congenital diaphragmatic hernia. *J. Pediatr. Surg.* **43**, 500-507. doi:10.1016/j.jpedsurg.2007.10.030

Nakamura, H., Doi, T., Puri, P. and Friedmacher, F. (2020). Transgenic animal models of congenital diaphragmatic hernia: a comprehensive overview of candidate genes and signaling pathways. *Pediatr. Surg. Int.* **36**, 991-997. doi:10.1007/s00383-020-04705-0

Nakazawa, N., Takayasu, H., Montedonico, S. and Puri, P. (2007). Altered regulation of retinoic acid synthesis in nitrofen-induced hypoplastic lung. *Pediatr. Surg. Int.* **23**, 391-396. doi:10.1007/s00383-006-1848-8

Nelson, C. M., Gleghorn, J. P., Pang, M.-F., Jaslove, J. M., Goodwin, K., Varner, V. D., Miller, E., Radisky, D. C. and Stone, H. A. (2017). Microfluidic chest cavities reveal that transmural pressure controls the rate of lung development. *Development* **144**, 4328-4335. doi:10.1242/dev.154823

Ng-Blichfeldt, J.-P., Schrik, A., Kortekaas, R. K., Noordhoek, J. A., Heijink, I. H., Hiemstra, P. S., Stolk, J., Königshoff, M. and Gosens, R. (2018). Retinoic acid signaling balances adult distal lung epithelial progenitor cell growth and differentiation. *EBioMedicine* **36**, 461-474. doi:10.1016/j.ebiom.2018.09.002

Nguyen, N. T. T., Contreras-Moreira, B., Castro-Mondragon, J. A., Santana-Garcia, W., Ossio, R., Robles-Espinoza, C. D., Bahin, M., Collombet, S., Vincens, P., Thieffry, D. et al. (2018). RSAT 2018: regulatory sequence analysis tools 20th anniversary. *Nucleic Acids Res.* **46**, W209-W214. doi:10.1093/nar/gky317

Nieto, M. A. (2013). Epithelial plasticity: a common theme in embryonic and cancer cells. *Science* **342**, 1234850. doi:10.1126/science.1234850

Nieto, M. A., Sargent, M. G., Wilkinson, D. G. and Cooke, J. (1994). Control of cell behavior during vertebrate development by Slug, a zinc finger gene. *Science* **264**, 835-839. doi:10.1126/science.7513443

Olver, R. E., Walters, D. V. and Wilson, S. M. (2004). Developmental regulation of lung liquid transport. *Annu. Rev. Physiol.* **66**, 77-101. doi:10.1146/annurev.physiol.66.071702.145229

Ono, K., Sandell, L. L., Trainor, P. A. and Wu, D. K. (2020). Retinoic acid synthesis and autoregulation mediate zonal patterning of vestibular organs and inner ear morphogenesis. *Development* **147**, dev192070. doi:10.1242/dev.192070

Pederiva, F., Martinez, L. and Tovar, J. A. (2012). Retinoic acid rescues deficient airway innervation and peristalsis of hypoplastic rat lung explants. *Neonatology* **101**, 132-139. doi:10.1159/000329613

Pereira-Terra, P., Moura, R. S., Nogueira-Silva, C. and Correia-Pinto, J. (2015). Neuroendocrine factors regulate retinoic acid receptors in normal and hypoplastic lung development. *J. Physiol.* **593**, 3301-3311. doi:10.1113/JP270477

Preibisch, S., Saalfeld, S. and Tomancak, P. (2009). Globally optimal stitching of tiled 3D microscopic image acquisitions. *Bioinformatics* **25**, 1463-1465. doi:10.1093/bioinformatics/btp184

Qiu, J., Nordling, S., Vasavada, H. H., Butcher, E. C. and Hirschi, K. K. (2020). Retinoic acid promotes endothelial cell cycle early G1 state to enable human hemogenic endothelial cell specification. *Cell Rep.* **33**, 108465. doi:10.1016/j.celrep.2020.108465

Rossant, J., Zirngibl, R., Cado, D., Shago, M. and Giguère, V. (1991). Expression of a retinoic acid response element-hsplacZ transgene defines specific domains of transcriptional activity during mouse embryogenesis. *Genes Dev.* **5**, 1333-1344. doi:10.1101/gad.5.8.1333

Sakai, T., Larsen, M. and Yamada, K. M. (2003). Fibronectin requirement in branching morphogenesis. *Nature* **423**, 876-881. doi:10.1038/nature01712

Savagner, P., Karavanova, I., Perantoni, A., Thiery, J. P. and Yamada, K. M. (1998). Slug mRNA is expressed by specific mesodermal derivatives during rodent organogenesis. *Dev. Dyn.* **213**, 182-187. doi:10.1002/(SICI)1097-0177(199810)213:2<182::AID-AJA3>3.0.CO;2-C

Schittny, J. C., Miserocchi, G. and Sparrow, M. P. (2000). Spontaneous peristaltic airway contractions propel lung liquid through the bronchial tree of intact and fetal lung explants. *Am. J. Respir. Cell Mol. Biol.* **23**, 11-18. doi:10.1165/ajrcmb.23.1.3926

Schmittgen, T. D. and Livak, K. J. (2008). Analyzing real-time PCR data by the comparative CT method. *Nat. Protoc.* **3**, 1101-1108. doi:10.1038/nprot.2008.73

Schneider, C. A., Rasband, W. S. and Eliceiri, K. W. (2012). NIH Image to ImageJ: 25 years of image analysis. *Nat. Methods* **9**, 671-675. doi:10.1038/nmeth.2089

Schuger, L., Varani, J., Mitra, R., Jr. and Gilbride, K. (1993). Retinoic acid stimulates mouse lung development by a mechanism involving epithelial-mesenchymal interaction and regulation of epidermal growth factor receptors. *Dev. Biol.* **159**, 462-473. doi:10.1006/dbio.1993.1256

Seamon, K. B., Padgett, W. and Daly, J. W. (1981). Forskolin: unique diterpene activator of adenylate cyclase in membranes and in intact cells. *Proc. Natl. Acad. Sci. USA* **78**, 3363-3367. doi:10.1073/pnas.78.6.3363

Shastry, S. M., Kolte, S. S. and Sanagapati, P. R. (2012). Potter's Sequence. *J Clin Neonatol* **1**, 157-159. doi:10.4103/2249-4847.101705

Smith, B. A., Tolloczko, B., Martin, J. G. and Grütter, P. (2005). Probing the viscoelastic behavior of cultured airway smooth muscle cells with atomic force microscopy: stiffening induced by contractile agonist. *Biophys. J.* **88**, 2994-3007. doi:10.1529/biophysj.104.046649

Squillacote, A. H. and Ahrens, J. (2006). *The ParaView guide*. Clifton Park, NY: Kitware.

Stuart, T., Butler, A., Hoffman, P., Hafemeister, C., Papalexi, E., Mauck, W. M., III, Hao, Y., Stoeckius, M., Smibert, P. and Satija, R. (2019). Comprehensive integration of single-cell data. *Cell* **177**, 1888-1902.e21. doi:10.1016/j.cell.2019.05.031

Swarr, D. T. and Morrisey, E. E. (2015). Lung endoderm morphogenesis: gasping for form and function. *Annu. Rev. Cell Dev. Biol.* **31**, 553-573. doi:10.1146/annurev-cellbio-100814-125249

Swift, J., Ivanovska, I. L., Buxboim, A., Harada, T., Dingal, P. C. D. P., Pinter, J., Pajerowski, J. D., Spinler, K. R., Shin, J.-W., Tewari, M. et al. (2013). Nuclear lamin-A scales with tissue stiffness and enhances matrix-directed differentiation. *Science* **341**, 1240104. doi:10.1126/science.1240104

Varner, V. D. and Nelson, C. M. (2014). Cellular and physical mechanisms of branching morphogenesis. *Development* **141**, 2750-2759. doi:10.1242/dev.104794

Varner, V. D., Gleghorn, J. P., Miller, E., Radisky, D. C. and Nelson, C. M. (2015). Mechanically patterning the embryonic airway epithelium. *Proc. Natl. Acad. Sci. USA* **112**, 9230-9235. doi:10.1073/pnas.1504102112

Vaughan, A. E. and Chapman, H. A. (2013). Regenerative activity of the lung after epithelial injury. *Biochim. Biophys. Acta* **1832**, 922-930. doi:10.1016/j.bbadis.2012.11.020

Vilos, G. A. and Liggins, G. C. (1982). Intrathoracic pressures in fetal sheep. *J. Dev. Physiol.* **4**, 247-256.

Wang, J., Ito, T., Udaka, N., Okudela, K., Yazawa, T. and Kitamura, H. (2005). PI3K-AKT pathway mediates growth and survival signals during development of fetal mouse lung. *Tissue Cell* **37**, 25-35. doi:10.1016/j.tice.2004.09.002

Warburton, D. (2021). Conserved Mechanisms in the Formation of the Airways and Alveoli of the Lung. *Front Cell Dev Biol* **9**, 662059. doi:10.3389/fcell.2021.662059

Wong, A. P., Shojaie, S., Liang, Q., Xia, S., Di Paola, M., Ahmadi, S., Bilodeau, C., Garner, J., Post, M., Duchesneau, P. et al. (2019). Conversion of human and mouse fibroblasts into lung-like epithelial cells. *Sci. Rep.* **9**, 9027; 9021-9015. doi:10.1038/s41598-019-45195-y

Wongtrakool, C., Malpel, S., Gorenstein, J., Sedita, J., Ramirez, M. I., Underhill, T. M. and Cardoso, W. V. (2003). Down-regulation of retinoic acid receptor α signaling is required for sacculation and type I cell formation in the developing lung. *J. Biol. Chem.* **278**, 46911-46918. doi:10.1074/jbc.M307977200

Xiao, Y., Hill, M. C., Zhang, M., Martin, T. J., Morikawa, Y., Wang, S., Moise, A. R., Wythe, J. D. and Martin, J. F. (2018). Hippo Signaling Plays an Essential Role in Cell State Transitions during Cardiac Fibroblast Development. *Dev. Cell* **45**, 153-169.e156. doi:10.1016/j.devcel.2018.03.019

Yang, Y., Relan, N. K., Przywara, D. A. and Schuger, L. (1999). Embryonic mesenchymal cells share the potential for smooth muscle differentiation: myogenesis is controlled by the cell's shape. *Development* **126**, 3027-3033. doi:10.1242/dev.126.13.3027

Yang, Y., Beqaj, S., Kemp, P., Ariel, I. and Schuger, L. (2000). Stretch-induced alternative splicing of serum response factor promotes bronchial myogenesis and is defective in lung hypoplasia. *J. Clin. Invest.* **106**, 1321-1330. doi:10.1172/JCI8893

Yi, L., Domyan, E. T., Lewandoski, M. and Sun, X. (2009). Fibroblast growth factor 9 signaling inhibits airway smooth muscle differentiation in mouse lung. *Dev. Dyn.* **238**, 123-137. doi:10.1002/dvdy.21831

Young, R. E., Jones, M.-K., Hines, E. A., Li, R., Luo, Y., Shi, W., Verheyden, J. M. and Sun, X. (2020). Smooth muscle differentiation is essential for airway size, tracheal cartilage segmentation, but dispensable for epithelial branching. *Dev. Cell* **53**, 73-85.e75. doi:10.1016/j.devcel.2020.02.001

Yue, F., Cheng, Y., Breschi, A., Vierstra, J., Wu, W., Ryba, T., Sandstrom, R., Ma, Z., Davis, C., Pope, B. D. et al. (2014). A comparative encyclopedia of DNA elements in the mouse genome. *Nature* **515**, 355-364. doi:10.1038/nature13992

Supplementary Figure 1

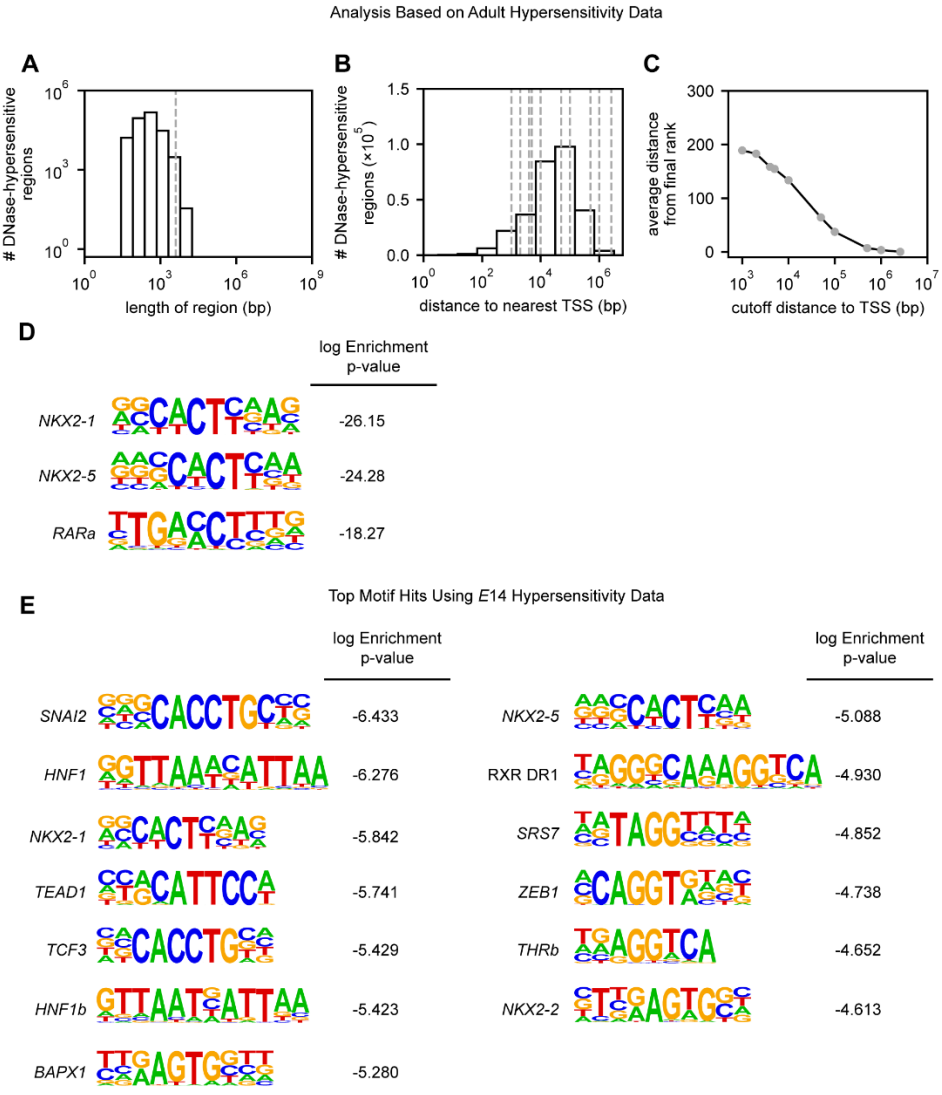

Fig. S1. Transcription-factor-binding motifs identified using a novel bioinformatics approach. **A)** Histogram of the lengths of all investigated DNase-hypersensitive regions from adult mouse lung ENCODE data. Dashed line shows the maximum length of a DNase-hypersensitive region that was included. **B)** Histogram of the distance of each DNase-hypersensitive region to the nearest TSS in the genome, using adult lung data. **C)** All identified TF motifs were ranked by their enrichment *p*-values in DNase-hypersensitive regions within different distances of the TSS in our dataset (corresponding to dashed lines in B). Datapoints represent the average difference in rank between TFs at each cutoff distance and their rank at the largest cutoff distance. **D)** Top three identified motifs using adult lung DNase-hypersensitivity data. **E)** Top 13 motifs identified using *E*14 lung DNase-hypersensitivity data. TSS, transcription start site; bp, base pairs; TF, transcription factor.

Supplementary Figure 2

A high ΔP

gene	log_2(fold change)	adjusted *p*
Rbp4	0.543	0.431
Stra6	-0.173	0.834
Rdh1	0.590	0.524
Rdh9	1.400	0.0789
Rdh10	-0.658	0.159
Rdh11	0.026	0.928
Rdh12	-0.244	0.672
Rdh13	-0.120	0.744
Dhrs3	-0.316	0.223
Hsd17b11	0.226	0.571
Bcmo1	0.195	0.855
Lrat	0.333	0.679
Aldh1a2 (Raldh2)	-0.361	0.492
Aldh1a3 (Raldh3)	-0.592	0.258
Cyp26a1	-0.721	0.376
Crabp2	-0.088	0.859
Nr2f2	0.105	0.784
Rara	-0.285	0.321
Rarb	-0.328	0.119
Rarg	0.019	0.981
Rxra	0.480	0.111
Rxrb	0.231	0.654
Rxrg	-0.907	0.0997

B epithelial *Yap* KO

gene	log_2(fold change)	adjusted *p*
Rbp2	-2.303	1
Rdh9	-0.468	1
Rdh11	0.152	0.228
Rdh12	0.373	0.284
Rdh13	0.011	0.93
Rdh14	0.143	0.368
Adh4	0.435	1
Hsd17b11	0.230	0.121
Hsd17b13	-0.960	1
Bcmo1	-1.066	1
Aldh1a2 (Raldh2)	0.006	0.957
Aldh1a3 (Raldh3)	-0.636	1
Aldh8a1	-1.002	1
Cyp26a1	1.240	1
Cyp26b1	-0.069	0.635
Cyp26c1	0.304	1
Rara	-0.032	0.779
Rarb	-0.077	0.524
Rxra	-0.062	0.548
Rxrb	-0.096	0.377
Rxrg	0.007	0.98

Fig. S2. Relative expression and adjusted *p* value of genes in the RA biosynthetic pathway that are differentially expressed **A)** under high ΔP or **B)** when *Yap* is deleted from the epithelium. See Figure 2C,E for significantly diferent pathway components and Figure 2D,F for volcano plots of these genes.

Supplementary Figure 3

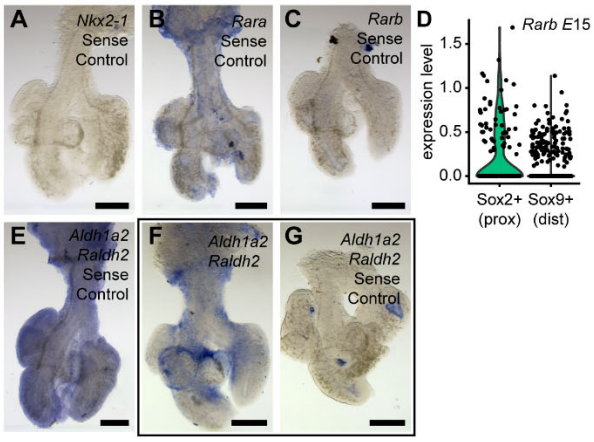

Fig. S3. Negative controls for *in situ* hybridization. Lungs incubated with positive sense (negative control) *in situ* hybridization probes for **A)** *Nkx2-1*, **B)** *Rara*, **C)** *Rarb*, and **E)** *Aldh1a2* developed in parallel with the explants shown in **Figure 3**. Lungs incubated with **F)** antisense and **G)** sense *in situ* hybridization probes for *Aldh1a2* for a shorter development time show a similar pattern of staining as in Figure 3H and very little sense staining compared to panel E. All scale bars, 250 μm. **D)** *Rarb* expression in scRNA-seq data from *E*15.5 airway epithelial cells. *Sox2* is expressed in the proximal (prox) airway epithelium and *Sox9* is expressed in the distal (dist) airway epithelium.

Supplementary Figure 4

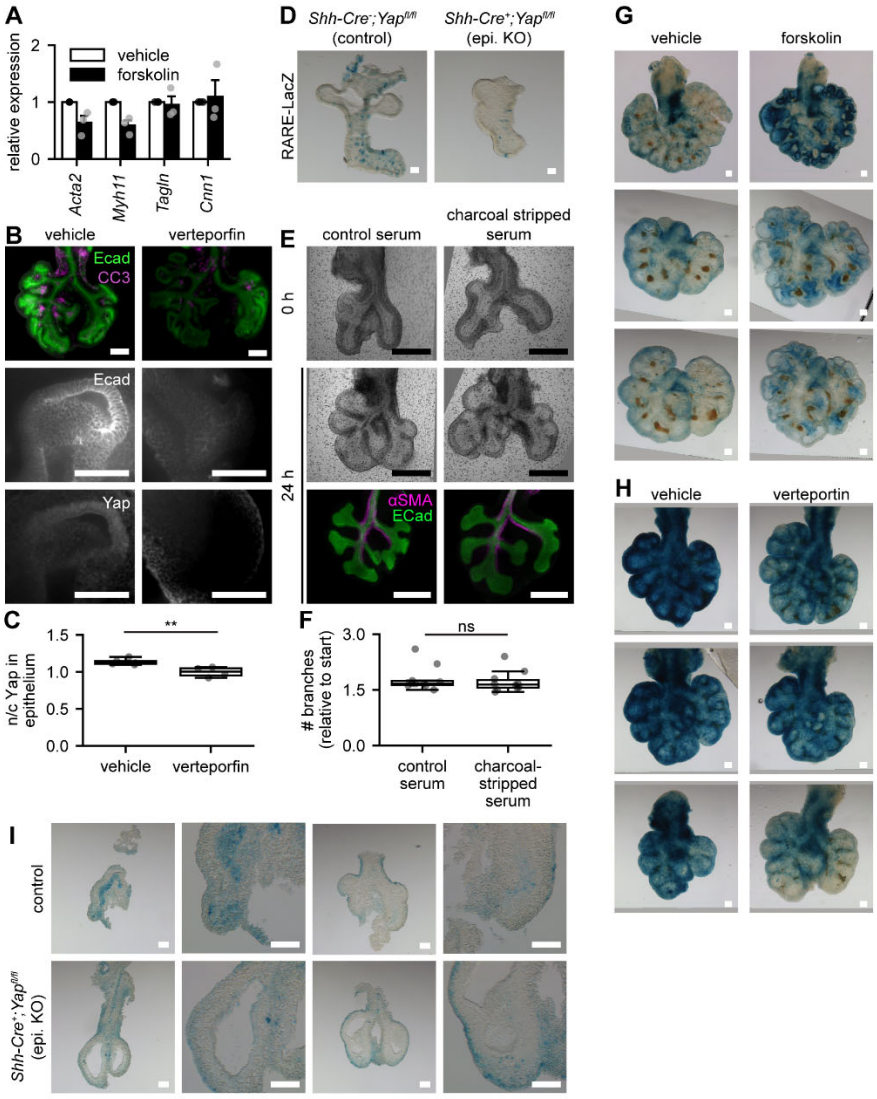

Fig. S4. Effects of forskolin, verteporfin, and *Yap* knockout on *E*11.5 lung explants. **A**) X-gal staining in *E*11.5 lungs explanted from *RARE-LacZ* reporter mice cultured in the presence of forskolin or vehicle control (DMSO) for 48 h. **B)** qRT-PCR analysis for smooth muscle gene markers in lungs cultured in the presence of forskolin or DMSO for 48 h. Shown are mean + s.e.m. Datapoints represent pooled RNA from 2-3 lungs from 3 independent experiments. **C)** Immunofluorescence analysis for Ecad, cleaved caspase 3 (CC3), and Yap in *E*11.5 lung explants cultured in the presence of verteporfin or vehicle control for 24 h. Scale bars: top row, 100 μm; bottom two rows, 50 μm. **D)** Quantification of the ratio of nuclear to cytoplasmic Yap staining in *E*11.5 lung explants cultured in the presence of verteporfin or vehicle control for 24 h. $p = 0.00700$ as denoted by Student's t-test. **E)** X-gal staining in *E*11.5 lungs explanted from *RARE-LacZ* reporter mice cultured in the presence of verteporfin or vehicle control (DMSO) for 48 h. X-gal staining in *E*11.5 *Shh-Cre;Yap$^{fl/fl}$;RARE-LacZ* epithelial *Yap* knockout (epi. KO) reporter **F**) lungs or **G**) mesenchyme-free epithelium. A, E, scale bars, 100 μm.

Supplementary Figure 5

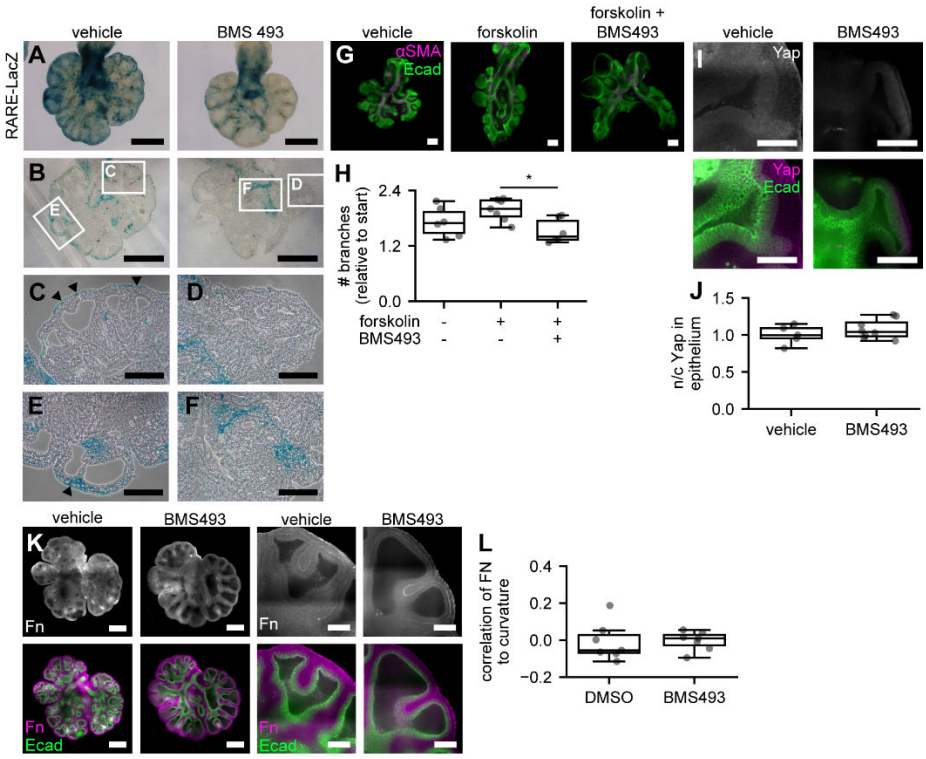

Fig. S5. Inhibiting RA signaling by treating RARE-LacZ reporter mouse lung explants with BMS493 decreases X-gal staining. **A)** Lungs cultured for 24 h in media supplemented with charcoal-stripped serum or non-charcoal stripped serum (control serum); brightfield scale bars, 500 μm; immunofluorescence scale bars, 250 μm. **B)** Relative change in the number of branches in *E*11.5 lung explants cultured in control medium or in medium containing charcoal-stripped serum for 24 h. X-gal stains of **C)** whole mounts and **D-H)** sections of lungs explanted from *RARE-LacZ* reporter mice cultured in the presence of BMS493 or vehicle control (DMSO) for 48 h. Scale bars: A, B 500 μm; C-F, 200 μm. Arrowheads indicate regions of darker X-gal stain in the mesothelium of controls. **I)** Immunofluorescence analysis for Yap and Ecad (scale bars, 50 μm) and **J)** quantification of the ratio of nuclear to cytoplasmic Yap in the epithelium in *E*11.5 lung explants cultured in the presence of BMS493 or vehicle control for 48 h. **K)** Immunofluorescence analysis for Ecad and αSMA and **L)** quantification of the number of epithelial branches in *E*11.5 lung explants cultured in the presence of forskolin, forskolin and BMS493, or vehicle control for 24 h. $p = 0.0250$ as denoted by one-way ANOVA, $p = 0.0201$ as denoted by Tukey's post-hoc test between lungs cultured in the presence of forskolin and lungs cultured in the presence of forskolin and BMS493. Scale bars, 100 μm.
M) Immunofluorescence analysis for fibronectin and Ecad (scale bars, left 200 μm; right 50 μm), and **N)** quantification of the correlation of fibronectin staining intensity to epithelial curvature in *E*11.5 lung explants cultured in the presence of BMS493 or vehicle control for 48 h.

Supplementary Figure 6

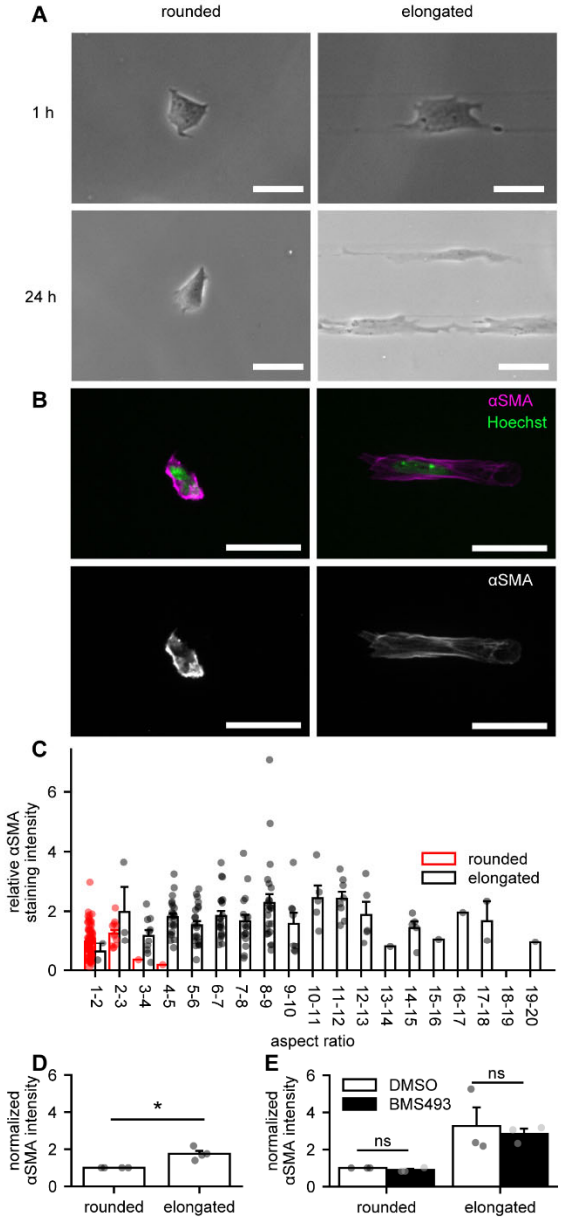

Fig. S6. Inhibiting RA signaling does not directly affect the differentiation of primary embryonic lung mesenchyme into smooth muscle cells. **A)** Phase-contrast images of cells on squares (rounded cells) or lines (elongated cells) of fibronectin after 1 h or 24 h of culture; scale bars, 50 µm. **B)** Immunofluorescence analysis for αSMA in rounded or elongated cells after 24 h of culture. Scale bars, 50 µm. **C)** Quantification of αSMA staining intensity in cells of different aspect ratios in panel B. Datapoints represent individual cells from 4 independent experiments. **D)** Quantification of average αSMA staining intensity in elongated versus rounded cells in panel B. Datapoints represent averages of all cells from each of 4 independent experiments. $p = 0.0189$ as denoted by Student's t-test. **E)** Quantification of αSMA staining intensity in rounded or elongated cells cultured with or without BMS493. Datapoints represent averages of all cells from each of 3 independent experiments. Shown are mean + s.e.m. ns, not significant.

Supplementary Figure 7

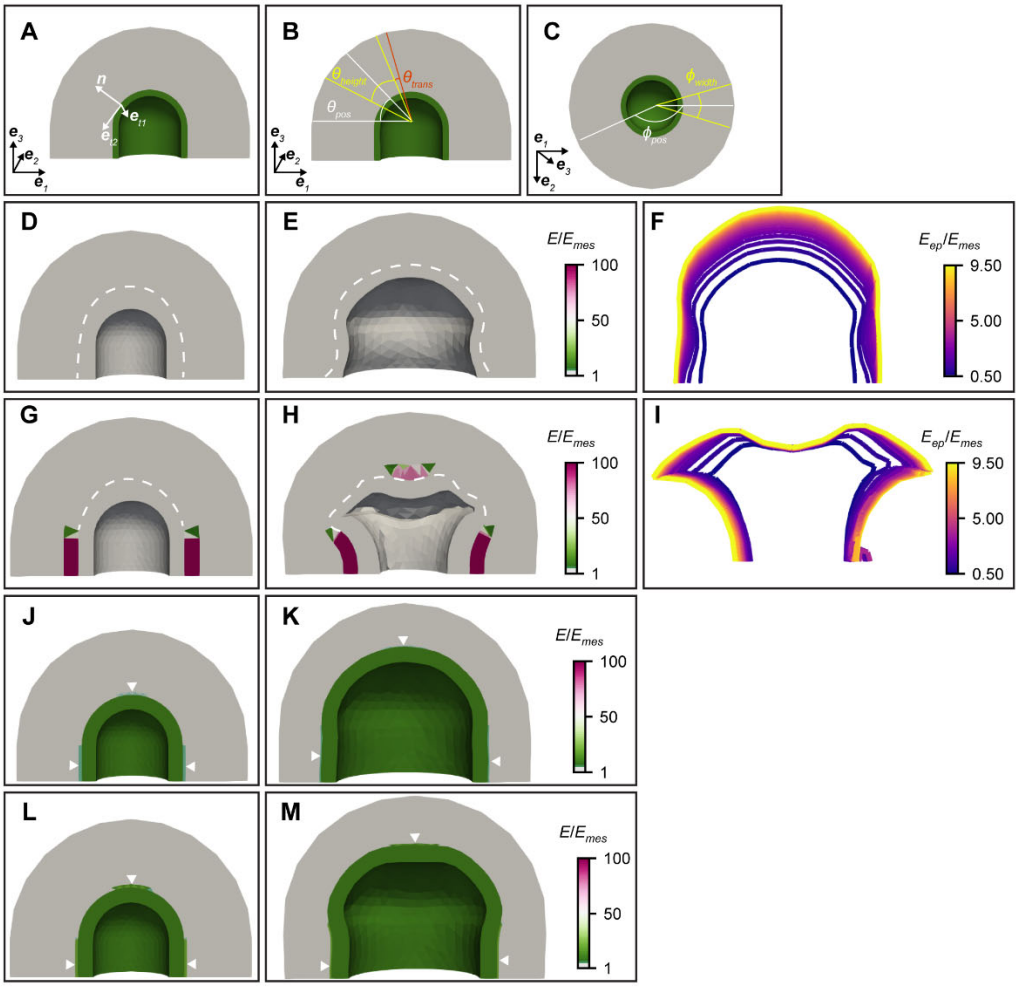

Fig. S7. Geometric parameters of the computational model. **A)** Epithelial coordinate system consisting of the normal vector and two tangent vectors to the epithelium. **B)** Angles in the $\boldsymbol{e_1}$-$\boldsymbol{e_3}$ plane between which epithelial proliferation is increased in models with increased proliferation along the flanks of the epithelium. **C)** Angles in the $\boldsymbol{e_1}$-$\boldsymbol{e_2}$ plane between which epithelial proliferation is increased in models with increased proliferation along the flanks of the epithelium. Initial geometries of simulations with $E_{ep} = E_{mes}$ and **D)** no ASM, or **G)** ASM. Initial geometries of simulations without ASM but with a thin layer of mesenchyme of stiffness **J)** $0.3E_{ep}$ or **L)** $2E_{ep}$ adjacent to the mesenchyme in a similar spatial pattern to the ASM of other models. **E, H, K, M)** Final geometries of simulations in panels D, G, J, and L respectively. Arrowheads in J, K, L, and M point to areas of increased mesenchymal stiffness. **F, I)** Final geometries of simulations using different epithelial stiffnesses for the classes of models represented by panels D and G, respectively.

Supplementary Figure 8

A

gene	log_2(fold change)	adjusted *p*	role in ASM differentiation
Shh	-2.757	5.00×10^{-5}	▲
Fgf9	0.201	0.279	▼
BMP4	0.583	5.00×10^{-5}	▲
Tgfb1	0.009	0.953	▲
Tgfb2	-0.911	5.00×10^{-5}	▲
Tgfb3	-1.122	5.00×10^{-5}	▲
Acta2	-1.064	5.00×10^{-5}	ASM marker
Actg2	-2.379	5.00×10^{-5}	ASM marker
Myh11	-2.175	5.00×10^{-5}	ASM marker
Tagln	-1.061	4.65×10^{-3}	ASM marker
Cnn1	-0.331	0.548	ASM marker
Cald1	-0.319	3.20×10^{-3}	ASM marker
Actn1	-0.196	0.0597	ASM marker
Actn2	3.371	5.00×10^{-5}	ASM marker
Actn3	0.945	4.05×10^{-3}	ASM marker
Actn4	-0.265	0.0104	ASM marker
Speg	0.382	0.0154	ASM marker
Lpp	0.263	0.0853	ASM marker
Srf	-0.057	0.851	ASM marker
Myocd	-1.279	5.00×10^{-5}	ASM marker
Mkl1	-0.115	0.384	ASM marker
Mkl2	0.431	5.00×10^{-5}	ASM marker
Lmod1	-2.214	5.00×10^{-5}	ASM marker
Des	1.103	5.00×10^{-5}	ASM marker
Vim	0.059	0.586	ASM marker
Vcl	-0.106	0.442	ASM marker
Mylk	-0.464	5.00×10^{-5}	ASM marker
Smtn	-0.354	1.45×10^{-3}	ASM marker
Heyl	-0.558	1.50×10^{-4}	ASM marker
Nog	-0.829	1.50×10^{-4}	ASM marker
Cspg4	0.080	0.592	ASM marker
Foxf1	-1.005	5.00×10^{-5}	ASM marker
Gata5	0.454	5.00×10^{-5}	ASM marker

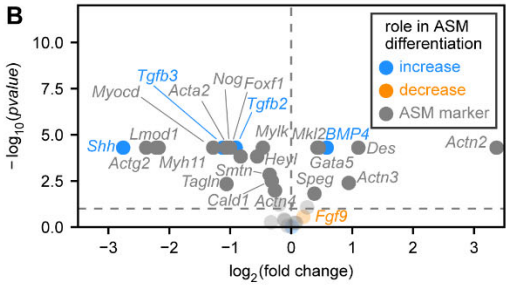

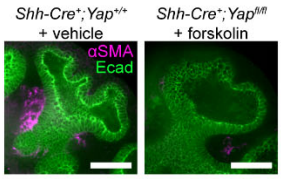

Fig. S8. Expression of ASM genes is modulated by Yap and ΔP. **A)** Relative expression, adjusted *p* value, and expected effect on ASM differentiation or marker status of ASM-controlling or marker genes that are significantly differentially expressed in the lung when *Yap* is conditionally knocked out in the airway epithelium. **B)** Volcano plot of the gene expression changes from A. **C)** Immunofluorescence analysis for αSMA and Ecad in *E*11.5 *Shh-Cre;Yap*$^{fl/fl}$ or littermate control lungs cultured in the presence of forskolin or vehicle control for 48 h. Scale bars, 50 µm.

Supplementary Figure 9

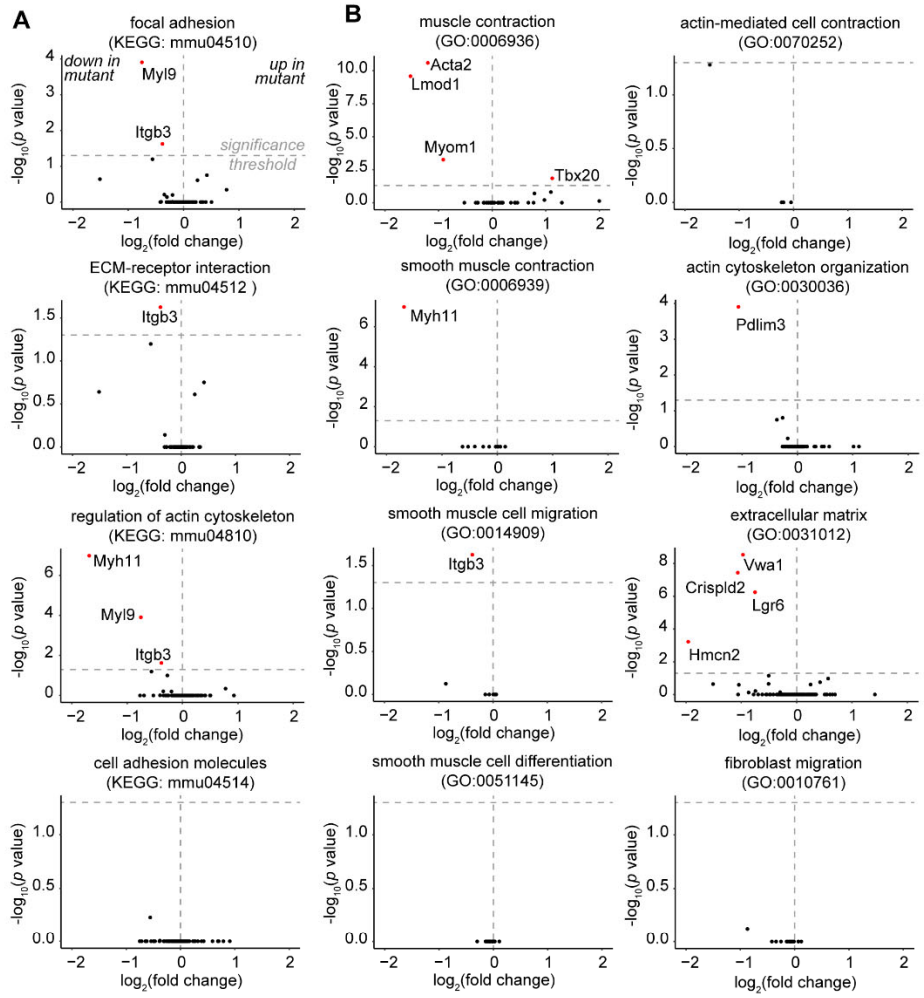

Fig. S9. *Myocd* knockout has a small effect on expression of genes involved in smooth muscle differentiation, ECM adhesion, and cytoskeletal organization. Volcano plots of relative expression and adjusted *p* value of genes involved in ECM deposition and adhesion and smooth muscle differentiation, cytoskeletal organization, and contraction from *E*13.5 lungs with mesenchymal *Myocd* knockout organized by the relevant **A)** Kyoto Encyclopedia of Genes and Genomes (KEGG) pathways and **B)** gene ontology (GO) groupings.

Table S1. Relative changes and *p*-values for differentially expressed genes in explanted *E*12.5 mouse lungs cultured under 200 or 20 Pa ΔP for 48 h, as described in (Nelson et al., 2017) Click here to download Table S1

Table S2. Primers used to genotype transgenic mice and embryos.

Gene	Sequence (5' → 3')	Reference
Yap^{fl}	F: AGGACAGCCAGGACTACACAG R: CACCAGCCTTTAAATTGAGAAC	Jackson Labs
Cre	F: GCATTACCGGTCGATGCAACGAGTGATGAG R: GAGTGAACGAACCTGGTCGAAATCAGTGCG	-
LacZ	F: ATCCTCTGCATGGTCAGGTC R: CGTGGCCTGATTCATTCC	Jackson Labs

Table S3. Primer sequences used for qRT-PCR.

Target	Symbol	Sequence (5' → 3')	Reference
18S ribosomal subunit	18S	F: TCAGATACCGTCGTAGTTC R: CCTTTAAGTTTCAGCTTTGC	(Lee et al., 2012)
α-smooth muscle actin	*Acta2*	F: GCATCCACGAAACCACCTA R: CACGAGTAACAAATCAAAGC	(Sousa et al., 2007)
transgelin	*Tagln*	F: TCCAGTCCACAAACGACCAAGC R: GAATTGAGCCACCTGTTCCATCTG	(Tanaka et al., 2008)
smooth muscle myosin heavy chain	*Myh11*	F: GCTAATCCACCCCCGGAGTA R: TCGCTGAGCTGCCCTTTCT	(Wilczewski et al., 2018)
calponin	*Cnn1*	F: ATGTCTTCTGCACATTTTAACC R: GCTCAAATCTCCGCTCTTG	(Hayashi et al., 2006)
serum response factor	*Srf*	F: GCTTCACCAGATGGCTGTGATA R: AATAAGTGGTGCCGTCCCTTG	(Schlesinger et al., 2011)
retinoic acid receptor-β	*Rarb*	F: TAGAAAACGACGACCCAGCA R: TGGGGTCAAGGGTTCATGTC	(Ng-Blichfeldt et al., 2018)

Table S4. Antibodies used for immunostaining.

Target	Species	Antibody Dilution	Source	Product Number
E-cadherin	Rabbit	1:200	Cell Signaling	24E10
E-cadherin	Rat IgG2a	1:200	ThermoFisher	13-1900
α-smooth muscle actin	Mouse	1:400	Millipore-Sigma	A5228
α-smooth muscle actin	Rabbit	1:200	Abcam	ab5694
Yap1	Rabbit	1:200	Novus Biologicals	NB110-58358
fibronectin	Rabbit	1:200	Sigma-Aldrich	F3648
cleaved caspase-3	Rabbit	1:200	Cell Signaling	9661S
anti-mouse alexa fluor 594	Goat	1:200	ThermoFisher	A11032
anti-mouse alexa fluor 647	Goat	1:200	ThermoFisher	A21235
anti-rabbit alexa fluor 488	Goat	1:200	ThermoFisher	A11034
anti-rabbit alexa fluor 594	Goat	1:200	ThermoFisher	A11012
anti-rabbit alexa fluor 647	Goat	1:200	ThermoFisher	A21245
anti-rat alexa fluor 488	Goat	1:200	ThermoFisher	A11006
anti-rat alexa fluor 594	Goat	1:200	ThermoFisher	A11007

Table S5. Primers used to generate probes for *in situ* hybridization.

Gene	Sequence (5' → 3')	Reference
Rara	F: ATGGGGTCAGCGCCTGTGAGG R: AGCGGCTCTTGCAGCATGTCC	-
Rarb	F: TGGAGTTCGTGGACTTTTCTG R: GCTCCGCTGTCATCTCATA	-
Nkx2-1 (*Ttf1*)	F: CAACAACTGCAGCAGGACAG R: GTCCGACCATAAAGCAAGGTAG	(Visel et al., 2004)
Aldh1a2 (*Raldh2*)	F: TGCTGATGTTCACCTGGAA R: TGCGGAGGATACCATGAG	-

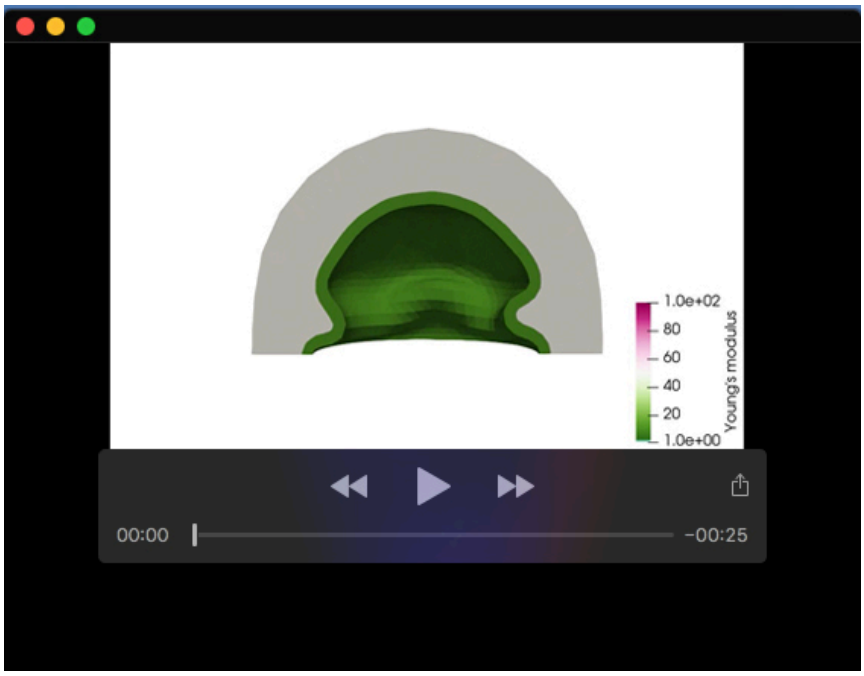

Movie 1. Computational model without smooth muscle. Related to Figure 6D,E.

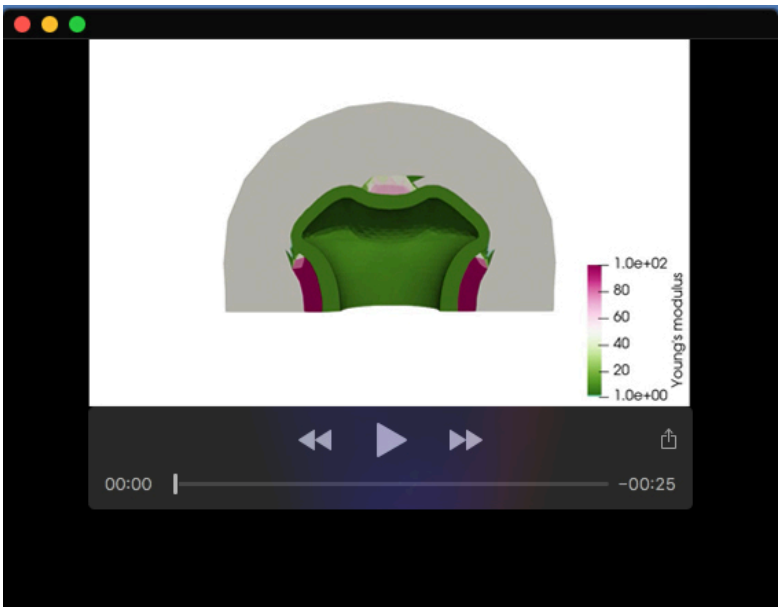

Movie 2. Computational model with smooth muscle. Related to Figure 6G,H.

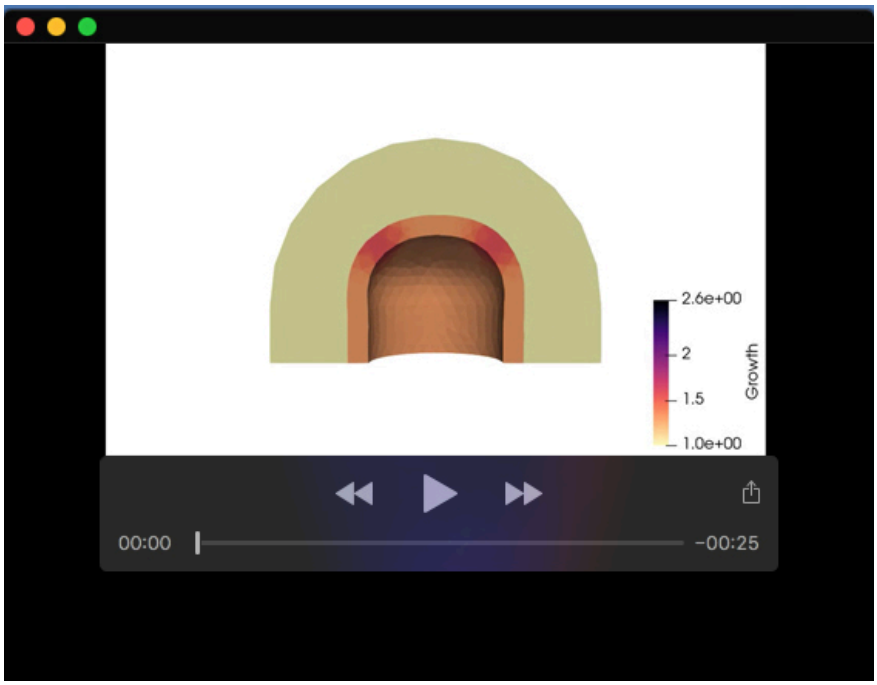

Movie 3. Computational model with increased growth along the flanks of the epithelium in a simulation with thick epithelium (t_{ep}/R_{out} = 0.12). Related to Figure 6J,K.

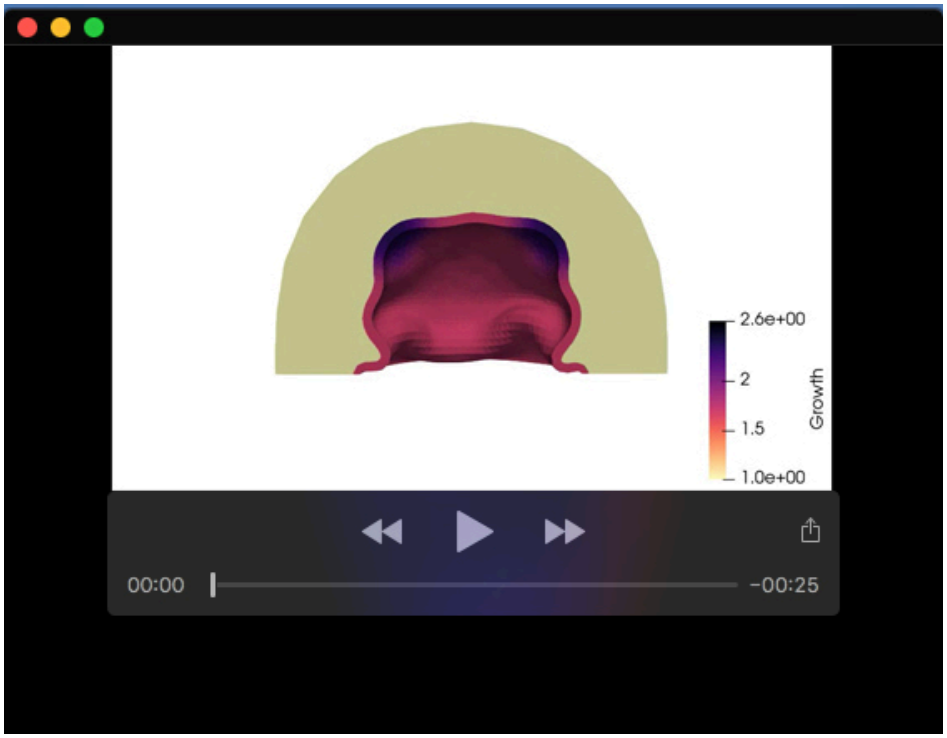

Movie 4. Computational model with increased growth along the flanks of the epithelium in a simulation with thin epithelium (t_{ep}/R_{out} = 0.05). Related to Figure 6J,L.

Supplementary Materials and Methods

Computational Model

We constructed a computational model, based on previous work (Goodwin et al., 2019; Nerger et al., 2021), of a growing epithelium surrounded by a stiff layer of smooth muscle to determine the relative roles of epithelial proliferation and smooth muscle differentiation in formation of epithelial cysts versus branches.

Geometry and physical properties

The geometry of the model consists of a short cylinder with a spherical cap on one end, comprising 3 layers around a central lumen, as shown in **Figure 6A-B**: an inner layer of epithelium surrounded by an incomplete layer of smooth muscle and an outer layer of mesenchyme, denoted as *ep*, *sm*, and *mes*, respectively. The smooth muscle wraps circumferentially around the cylindrical part of the epithelium and forms a strap around the tip of the spherical epithelial cap (**Figure 6B**).

The thicknesses of the epithelial and smooth muscle layers are denoted as t_{ep} and t_{mus}, respectively, and the overall radius of the model is denoted as R_{out}. The relative thicknesses of the layers in the model, in particular the ratio of t_{ep}/R_{out}, are based on our experimental measurements (**Figure 6B-C**).

Mechanical model

We follow (Rodriguez et al, 1994) to model tissue growth, where the shape change of tissues from the reference state is considered to be due to a combination of growth and elastic deformation. The system is assumed to be in quasi-mechanical equilibrium, since mechanical

relaxation is much faster than the processes of epithelial growth and smooth muscle differentiation. The equilibrium state can be obtained by the following energy-minimizing procedures:

Suppose that the tissue initially occupies a volume Ω in a 3D Euclidian space, with a fixed Cartesian coordinate (X_1, X_2, X_3) and an orthonormal basis $(\boldsymbol{e}_1, \boldsymbol{e}_2, \boldsymbol{e}_3)$. After some time *t*, the volume of the tissue turns into Ω_t and for each point in the reference volume, its Cartesian coordinates $\boldsymbol{X} = X_i\, \boldsymbol{e}_i$ get mapped into a difference vector $\boldsymbol{x} = x_i\, \boldsymbol{e}_i$ (summation over repeated indices is implied), and we denote such mapping as $\boldsymbol{x} = \boldsymbol{\varphi}(\boldsymbol{X})$.

Following (Ogden, 1997), shape transformation from the reference state can be described by the deformation gradient tensor $\boldsymbol{F} = \frac{\partial \boldsymbol{x}}{\partial \boldsymbol{X}}$ and, following (Rodriguez et al, 1994), we adopt the so-called multiplicative decomposition: $\boldsymbol{F} = \boldsymbol{F}^e \boldsymbol{F}^g$. This decomposition essentially assumes that the tissue first grows to an intermediate stress-free state due to $\boldsymbol{F}^g$ (often referred to as the growth tensor) and then to the final state by an additional elastic deformation due to $\boldsymbol{F}^e$. It is often more convenient to work with the displacement field $\boldsymbol{u} \equiv \boldsymbol{x} - \boldsymbol{X}$ and, hence, $\boldsymbol{F} = \boldsymbol{I} + \frac{\partial \boldsymbol{u}}{\partial \boldsymbol{X}}$ with $\boldsymbol{I}$ being the identity tensor.

We model all three layers as neo-Hookean hyperelastic solids, with the following strain energy density function (Ogden, 1997):

$$\psi\left(\boldsymbol{F}^e = \boldsymbol{F}\boldsymbol{F}^{g^{-1}}\right) = \frac{\mu}{2}(I_C^e - 3) - \mu \ln(J^e) + \frac{\lambda}{2}\ln(J^e)^2, \qquad (1)$$

where $J^e = \det(\boldsymbol{F}^e)$, $I_{\boldsymbol{C}}^e = \mathrm{trace}(\boldsymbol{C})$ and $\boldsymbol{C} = (\boldsymbol{F}^e)^T\,\boldsymbol{F}^e$ is the right Cauchy-Green tensor. λ and μ are Lamé parameters, which are related to the Young's modulus E and Poisson ratio ν through:

$$\lambda = \frac{E\nu}{(1+\nu)(1-2\nu)}, \qquad \mu = \frac{E}{2(1+\nu)}. \tag{2A,B}$$

The relative Young's moduli were estimated as reported in **Figure 6C**, and ν = 0.4 is assumed for all three layers. Gmsh was used to create a linear tetrahedral mesh for applying the finite element method (FEM) to the geometry (Geuzaine and Remacle, 2009).

Growth tensor

The growth tensor $\boldsymbol{F}^g$ uniquely determines the shape transformation due to growth. For simplicity, we assume that the undifferentiated mesenchyme and smooth muscle tissues do not grow, i.e., $\boldsymbol{F}_{mes}^g = \boldsymbol{F}_{sm}^g = \boldsymbol{I}$. Based on experimental observations, we consider the following growth tensor for the epithelium:

$$\boldsymbol{F}_{ep}^g = \boldsymbol{n} \otimes \boldsymbol{n} + g\boldsymbol{e}_{t_1} \otimes \boldsymbol{e}_{t_1} + g\boldsymbol{e}_{t_2} \otimes \boldsymbol{e}_{t_2}, \tag{3}$$

where $\boldsymbol{n}$ is the outer normal vector, and $\boldsymbol{e}_{t_1}$ and $\boldsymbol{e}_{t_2}$ are the tangent vectors of the epithelium (**Figure S7A**). At the beginning of the simulation $g = 1$. g then increases linearly for 10 timesteps until $g = 2$.

In simulations of spatially-patterned proliferation, the total growth of the epithelium g_{tot} is

$$g_{tot} = g + (g-1)\left(g_{region_1} + g_{region_2}\right) \tag{4}$$

where

$$g_{region_i} = \left(\frac{1 + \tanh\left(\frac{\phi - \frac{\phi_{pos_i} - \phi_{width}}{2}}{\theta_{trans}} \right) \tanh\left(\frac{\frac{\phi_{pos_i} + \phi_{width}}{2} - \phi}{\theta_{trans}} \right)}{2} \right) \left(\frac{1 + \tanh\left(\frac{\theta - \frac{\theta_{pos} - \theta_{height}}{2}}{\theta_{trans}} \right) \tanh\left(\frac{\frac{\theta_{pos} + \theta_{height}}{2} - \theta}{\theta_{trans}} \right)}{2} \right) \quad (5)$$

where ϕ is the azimuth angle and θ is the inclination angle and $\phi_{pos1} = 0$, $\phi_{pos2} = \pi$, $\phi_{width} = \frac{\pi}{3}$, $\theta_{pos} = \frac{\pi}{4}$, $\theta_{height} = \frac{\pi}{6}$, and $\theta_{trans} = 0.15$ (**Figure S7B-C**).

ASM differentiation

In simulations including smooth muscle, the smooth muscle wrapped around the tip of the epithelium (**Figure 6B**, red dashed box) begins the simulation with stiffness E_{mes} and increases in stiffness linearly throughout simulation time until it reaches E_{mus} at the end of the simulation. In simulations in which we modify the rate of ASM differentiation relative to epithelial proliferation, smooth muscle stiffness increases linearly but more slowly, such that at the end of simulation time the stiffness is E_{final}, where the color bar in **Figure 7C** represents $\frac{E_{final}/E_{mus}}{g_{final} - g_{initial}}$, where $g_{initial} = 1$ and $g_{final} = 2$, as defined above. The smooth muscle around the flanks of the epithelium (**Figure 6A**, magenta) has modulus E_{mus} throughout all simulations.

Boundary conditions

The bottom surface of the model $\partial\Omega_b$ has a fixed displacement $u_3 = 0$. The displacement of the point at the distal tip of the top of the mesenchyme has a fixed displacement of $u_1 = u_2 = 0$ to prevent translation of the structure, and a point on $\partial\Omega_b$ on the outer circumference of the mesenchyme has a fixed displacement of $u_2 = 0$ to prevent rotation of the structure.

The outside surface of the mesenchyme is considered traction-free, but the inner surface of the epithelium, $\partial\Omega^{in}$, has a positive pressure opposite to the normal vector $\boldsymbol{n}$ at every point such that the traction force $\boldsymbol{t}$:

$$\boldsymbol{t} = -p\boldsymbol{n}, \tag{6}$$

where $p = 0.1E_{mes}$ (Chevalier et al., 2016; Nelson et al., 2017). And $\boldsymbol{n}$ is the outer normal vector of $\partial\Omega^{in}$ in the deformed state.

Finite element method

The equilibrium state of the system at each time step can be determined by obtaining the stationary point of the following potential energy function (Dervaux and Ben Amar, 2011):

$$\Pi = \int_{\Omega} J^{g}\psi(\boldsymbol{F}^{e})\ dX - \int_{\Omega} \boldsymbol{B}\cdot\boldsymbol{u}\, dX - \int_{\partial\Omega_{t}^{in}} \boldsymbol{t}\cdot\boldsymbol{u}\, ds, \tag{7}$$

where Ω is the whole domain of the reference state, dX is an infinitesimal volume element of the domain, $\boldsymbol{B} = 0$ everywhere on Ω because no body-force is applied to the structure, $\partial\Omega_{t}^{in}$ represents the luminal boundary of the epithelium in the deformed configuration, and ds is an infinitesimal element of the boundary in the deformed state. The stationary point of the above potential energy can be obtained by solving the following equation:

$$0 = \delta\Pi = \delta\int_{\Omega} J^{g}\psi(\boldsymbol{F}^{e})\ dX + \int_{\partial\Omega^{in}} p\,\boldsymbol{n}\cdot\delta\boldsymbol{u}\, dS \tag{8A}$$

$$= \delta\int_{\Omega} J^{g}\psi(\boldsymbol{F}^{e})\ dX + \int_{\partial\Omega^{in}} p(J\boldsymbol{F}^{-T}\boldsymbol{N})\cdot\delta\boldsymbol{u}\, dS \tag{8B}$$

where $\partial\Omega^{in}$ and dS are the luminal boundary and the infinitesimal surface elements of the luminal boundary of the undeformed epithelial domain, respectively.

We used the FEM to solve the above minimization problem numerically (Bathe, 1996). Using the tetrahedral mesh generated by Gmsh to discretize the domain Ω, we solved for $\boldsymbol{u}$ at each timestep using the open-source FEniCS software (Logg et al., 2012) to apply the Newton-Raphson algorithm (Atkinson, 1989) in each element of the mesh. Where the Newton-Raphson algorithm failed to converge, we applied the dynamic relaxation method (Underwood, 1983) to find the $\boldsymbol{u}$ that minimized the problem. The results were visualized in the open-source tool Paraview (Squillacote and Ahrens, 2006).

The solution was tested to be robust to mesh refinements. The basic physics of the simulation was tested by inspecting the results of simulations with pressure in the lumen but without epithelial growth to ensure the model expanded in this case as expected.

Supplementary References

Atkinson, K. E. (1989). *An introduction to numerical analysis* (2nd edn). New York: Wiley.

Bathe, K.-J. (1996). *Finite element procedures*. Englewood Cliffs, N.J.: Prentice Hall.

Chevalier, N. R., Gazquez, E., Dufour, S. and Fleury, V. (2016). Measuring the micromechanical properties of embryonic tissues. *Methods* **94**, 120-128.

Dervaux, J. and Ben Amar, M. (2011). Buckling condensation in constrained growth. *J. Mech. Phys. Solids* **59**, 538-560.

Geuzaine, C. and Remacle, J. F. (2009). Gmsh: A 3-D finite element mesh generator with built-in pre- and post-processing facilities. *Int. J. Numer. Meth. Eng.* **79**, 1309-1331.

Goodwin, K., Mao, S., Guyomar, T., Miller, E., Radisky, D. C., Kosmrlj, A. and Nelson, C. M. (2019). Smooth muscle differentiation shapes domain branches during mouse lung development. *Development* **146**, 1-13.

Hayashi, K., Nakamura, S., Nishida, W. and Sobue, K. (2006). Bone morphogenetic protein-induced MSX1 and MSX2 inhibit myocardin-dependent smooth muscle gene transcription. *Mol Cell Biol* **26**, 9456-9470.

Lee, K., Chen, Q. K., Lui, C., Cichon, M. A., Radisky, D. C. and Nelson, C. M. (2012). Matrix compliance regulates Rac1b localization, NADPH oxidase assembly, and epithelial-mesenchymal transition. *Mol. Biol. Cell* **23**, 4097-4108.

Logg, A., Mardal, K.-A. and Wells, G. (2012). *Automated Solution of Differential Equations by the Finite Element Method : The FEniCS Book*. Heidelberg: Springer.

Nelson, C. M., Gleghorn, J. P., Pang, M. F., Jaslove, J. M., Goodwin, K., Varner, V. D., Miller, E., Radisky, D. C. and Stone, H. A. (2017). Microfluidic chest cavities reveal that transmural pressure controls the rate of lung development. *Development* **144**, 4328-4335.

Nerger, B. A., Jaslove, J. M., Elashal, H. E., Mao, S., Kosmrlj, A., Link, A. J. and Nelson, C. M. (2021). Local accumulation of extracellular matrix regulates global morphogenetic patterning in the developing mammary gland. *Curr. Biol.*, 1-15.

Ng-Blichfeldt, J. P., Schrik, A., Kortekaas, R. K., Noordhoek, J. A., Heijink, I. H., Hiemstra, P. S., Stolk, J., Konigshoff, M. and Gosens, R. (2018). Retinoic acid signaling balances adult distal lung epithelial progenitor cell growth and differentiation. *EBioMedicine* **36**, 461-474.

Ogden, R. W. (1997). *Non-linear elastic deformations*. Mineola, N.Y.: Dover Publications.

Schlesinger, J., Schueler, M., Grunert, M., Fischer, J. J., Zhang, Q., Krueger, T., Lange, M., Tonjes, M., Dunkel, I. and Sperling, S. R. (2011). The cardiac transcription

network modulated by Gata4, Mef2a, Nkx2.5, Srf, histone modifications, and microRNAs. *PLoS Genet.* **7**, e1001313; 1001311-1001316.

Sousa, A. M., Liu, T., Guevara, O., Stevens, J., Fanburg, B. L., Gaestel, M., Toksoz, D. and Kayyali, U. S. (2007). Smooth muscle alpha-actin expression and myofibroblast differentiation by TGFbeta are dependent upon MK2. *J. Cell. Biochem.* **100**, 1581-1592.

Squillacote, A. H. and Ahrens, J. (2006). *The ParaView guide*. Clifton Park, NY: Kitware.

Tanaka, T., Sato, H., Doi, H., Yoshida, C. A., Shimizu, T., Matsui, H., Yamazaki, M., Akiyama, H., Kawai-Kowase, K., Iso, T., et al. (2008). Runx2 represses myocardin-mediated differentiation and facilitates osteogenic conversion of vascular smooth muscle cells. *Mol Cell Biol* **28**, 1147-1160.

Underwood, P. (1983). Dynamic Relaxation. In *Computational methods for Transient Analysis* (ed. T. Belytschko & T. J. R. Hughes), pp. 245-265. Amsterdam Netherlands: North-Holland Pub.

Visel, A., Thaller, C. and Eichele, G. (2004). GenePaint.org: an atlas of gene expression patterns in the mouse embryo. *Nucleic Acids Res.* **32**, D552-556.

Wilczewski, C. M., Hepperla, A. J., Shimbo, T., Wasson, L., Robbe, Z. L., Davis, I. J., Wade, P. A. and Conlon, F. L. (2018). CHD4 and the NuRD complex directly control cardiac sarcomere formation. *Proc. Natl. Acad. Sci. U. S. A.* **115**, 6727-6732.